https://doi.org/10.1021/acs.energyfuels.3c02432

Elucidating the Effect of Crystallinity on Photoactivity in Poly(heptazine imides)

Junyi Li,[a] Jesús Barrio,[b] Yuanxing Fang,[c] Yongxin Pan,[c] Michael Volokh,[a] Sanjit Mondal,[a] Jonathan Tzadikov,[a] Liel Abisdris,[a] Ayelet Tashakory,[a] Xinchen Wang,[c] Xirui Zhang*[c] and Menny Shalom*[a]*

a. Department of Chemistry and Ilse Katz Institute for Nanoscale Science and Technology, Ben-Gurion University of the Negev, Beer-Sheva 8410501, Israel. E-mail: mennysh@bgu.ac.il

b. Department of Chemical Engineering, Imperial College London, Royal School of Mines, London SW72AZ, England, UK. E-mail: j.barrio-hermida@imperial.ac.uk

c. State Key Laboratory of Photocatalysis on Energy and Environment, College of Chemistry, Fuzhou University, Fuzhou, 350116 P. R. China. E-mail: dardons@126.com

ABSTRACT: Poly(heptazine imides) (PHI) polymers have been widely studied owing to their excellent activity as photocatalysts for various reactions. Their photocatalytic activity has been attributed to defects, optical adsorption, or synergistic effects with ions in the reaction media. However, the role of PHI's crystal structure on photocatalytic activity has not been elucidated. Herein, we reveal a direct correlation between the photocatalytic production of hydrogen (H_2) and the crystal structure of PHI. We synthesized polymeric carbon nitrides materials focusing on different PHI (001)/(002) crystal plane ratios, high specific surface area, and enhanced light response by co-polymerizing organic monomers in a KCl/LiBr molten salt medium. Theoretical and experimental results disclose that the charge carrier dynamics and electron mobility govern the photoactivity of PHI. The best photocatalyst, which had the highest abundance of PHI (100) planes, showed state-of-the-art performance for the hydrogen evolution reaction, with apparent quantum efficiencies of 15.6% at 405 nm and 1.32% at 595 nm, and for the production of H_2O_2 in pure water under visible light (66.7 μmol g^{-1} h^{-1}).

KEYWORDS: Poly(heptazine imides), crystal structure, photocatalysis, hydrogen evolution, hydrogen peroxide production.

1. INTRODUCTION

Crystalline carbon nitride materials (CNs) such as poly(heptazine imides) (PHI) and poly(triazine imide) (PTI) have emerged as highly active photocatalysts for various reactions, including water splitting,[1–5] CO_2 reduction,[6–8] hydrogen peroxide synthesis,[9–11] and organic transformation reactions.[12–14] Their high activity compared to that of traditional CNs,[5,15–18] is due to better light-harvesting properties, high specific surface area, suppressed recombination under illumination, and better charge mobility.[3,19] The synthesis of CNs with high crystallinity is typically achieved by using molten salts as the reaction medium.[20] The final composition and structure are usually determined by how the salt ions are stabilized at the high temperatures where the CN formation reaction takes place. The reaction temperature, the identity of the ions of the eutectic mixture,[21] and the employed CN monomers[22–24] direct the condensation path and therefore the structure of the final CN.

Very recently, Lin et al. noted that the photocatalytic performance of crystalline PTI materials depends on the exposed reactive facets.[25] They have shown that the side prismatic planes {100} in poly(triazine imides) (specifically, PTI/Li^+Cl^-) are the most reactive facets because the employed co-catalyst is preferentially photodeposited on their surface and the migration of photogenerated electron–hole pairs occurs faster on these facets. In fact, Lin et al. showed that the photocatalytic

activity is linearly correlated with the surface area ratio of the {100} and {001} facets of the PTI/Li^+Cl^- crystals.[25]

In general, PHI exhibits higher photoactivity than PTI thanks to its better light-harvesting ability stemming from its larger π-conjugated system.[26] The greater activity of PHI was attributed to better optical absorption,[27] the degree of condensation,[28] the presence of defects[29] or cyanamide moieties in the material, [30,31] or the presence of hydrated cations in the reaction media.[32–34] However, PHI's most reactive facet and the influence of its crystallinity and crystal structure on photocatalytic activity have not been identified to date.

Here, we elucidated the dependence of the photocatalytic activity of PHI-based materials on their crystal structure and observed a linear correlation between the photocatalytic production of hydrogen and hydrogen peroxide and the ratio of the (100) and (002) signal intensities in their X-ray diffraction patterns, in contrast to what was observed for PTI-based materials.[25] We prepared a set of crystalline PHI-based CN materials by co-polymerization of different C,N precursors in a KCl/LiBr molten salt medium. The PHI-based materials show enhanced optical absorption thanks to the use of carbon-rich molecules—barbituric acid (BA)[35] or 2,4,6-triaminopyirimidine (TAP)[36]—as comonomers of dicyandiamide (DCD) during the synthesis.[37] Their crystal structure and chemical composition were elucidated using of X-ray diffraction (XRD), X-ray photoelectron spectroscopy (XPS), and transmission electron microscopy (TEM), among others. Furthermore, to understand the charge carrier dynamics on different crystal planes

of PHI materials density functional theory (DFT) calculations were employed in conjunction with photoluminescence (PL) and photoelectrochemical measurements.

2. EXPERIMENTAL SECTION

2.1 Sample preparation

The used chemicals and substrates, their purity, and commercial vendors is listed in the Supporting Information. PHI materials were prepared by pyrolysis of a mixture of dicyandiamide (DCD) and different quantities of barbituric acid (BA) in a KCl/LiBr eutectic medium at 500 °C for 4 h using different salt:reactants mass ratios (DCDBA*x*, *x* = 2, 5, 10, 20, where *x* is the mass of salt relative to the mass of the precursor mixture). Typically, 0.91 g DCD and 0.09 g BA (i.e., BA:DCD mole ratio = 1:15) were used as the precursors, and 5.00 g eutectic mixture of KCl/LiBr salts (1:3 mass ratio, melting point: 263 °C) served as the reaction medium. DCD, BA, and the salt medium were ground with an agate mortar and pestle. This mixture was placed in a ceramic lidded crucible, followed by heating to the target temperature of 500 °C for a 4 h reaction, in a muffle furnace under atmospheric conditions. The product powder (removed from the furnace after colling down to ambient temperature) underwent a series of washes using distilled water to eliminate residual salts. Finally, after a drying stage at 40 °C for 8 h, these powders were collected for further characterization and use in photocatalytic reactions.

To explore the possibility of adapting the reported synthetic approach to a wider variety of precursors, we replaced BA with 2,4,6-triaminopyrimidine (TAP), an organic monomer

commonly employed to increase the C-to-N ratio in synthesized CN materials. As in the previous synthesis, PHI materials were prepared by pyrolysis of dicyandiamide (DCD) with different amounts of TAP in a KCl/LiBr eutectic medium at 500 °C for 4 h using different salt:reactants mass ratios (DCDTAP*x*, *x* = 2, 5, 10, 20, where *x* is the mass of salt relative to the mass of the precursor mixture).

To study the correlation between chemical composition and photocatalytic performance, the effect of the relative amounts of BA and TAP in the precursor mixture on the structure and photocatalytic activities of the ensuing CN materials was studied by changing the BA (or TAP)-to-DCD molar ratio in the precursor (namely 1:30, 1:15, 1:10).

To study the formation mechanism of (100) plane-rich PHI CN materials, samples were prepared in the absence of a eutectic medium (calcination of a mixture of DCD and BA only) or from the ionothermal pyrolysis of DCD as the sole component of the precursor.

In addition, for the comparison of H_2O_2 production performance, bulk CN was synthesized via direct solid-state thermal condensation reaction: 5.00 g DCD was positioned within a lidded crucible and a temperature ramp was applied—gradual heating at a rate of 4 °C min^{-1} until reaching 500 °C—followed by residence time of 4 h at the target temperature, and cooling down back to ambient conditions. The resulting yellow powder was processed into a fine powdered state (using an agate mortar and pestle). The full list of characterization apparatus is listed in the Supporting Information.

2.2 Photocatalytic experiments

Thermostatically-controlled hydrogen evolution reaction (HER) measurements were

performed under white LED visible-range illumination in accordance to a previous report from our group in the presence of a Pt co-catalyst and triethanolamine (TEOA) hole scavengers.[38] (see detailed description in the Supporting Information).

Photocatalytic O_2 reduction reaction (ORR) experiments to produce H_2O_2 were carried out in pure water (without co-catalysts or scavengers) at 30 °C. The hydrogen peroxide product amount was colorimetrically determined using an aqueous potassium permanganate solution following published standard procedures.[39,40] The detailed description of photocatalytic HER and ORR reactions and product quantification is elaborated in the Supporting Information.

2.3 DFT calculations

All density functional theory (DFT) calculations employed the Vienna ab-initio simulation package (VASP) code.[41] Nuclei and core electrons were described by projector augmented wave (PAW) potentials.[42] The generalized gradient approximation of Perdew–Burke–Ernzerhof (PBE) exchange-correlation functional was used combined with Grimme's DFT-D3 correction.[43–45] Monkhorst–Pack meshes of 3×2×6, 2×2×6, and 3×3×6 *k*-points were used in the Brillouin zone for geometry optimizations and electronic structure calculations of bulk CN, PTI (2×2×1 supercell), and PHI, respectively. The cut-off energy of the plane-wave expansion was set to 550 eV, and the convergence thresholds of the energy change and the maximum force were set to 10^{-5} eV and 0.01 eV $Å^{-1}$, respectively. A 15 Å vacuum space was set to avoid neighboring layers interactions. The carrier effective mass (m^*) is calculated using the relation $E = \hbar^2k^2/2m$ based on the energy band structure.

According to the equation $\mu = \tau e/m^*$, the mobility (μ) is proportional to the mean free time of the carrier (τ) and the elementary charge (e) and proportional to the inverse carrier effective mass (m^{*-1}).

3. RESULTS AND DISCUSSION

3.1 Materials synthesis and characterization

PHI materials were synthsized using DCD pyrolysis with different amounts of BA in a KCl/LiBr eutectic medium at 500 °C for 4 h using different salt:reactants ratios (**Scheme 1**); the resulting samples were marked as DCDBA*x*, *x* standing for the salt:reactants mass ratio (for the sake of readability, in the figures, they are simply identified by their *x* ratio; e.g., DCDBA20 designates a 20:1 ratio). The eutectic mixture KCl/LiBr was chosen for its low eutectic temperature of 263 °C,[46] which is in proximity to the DCD melting point (211 °C).

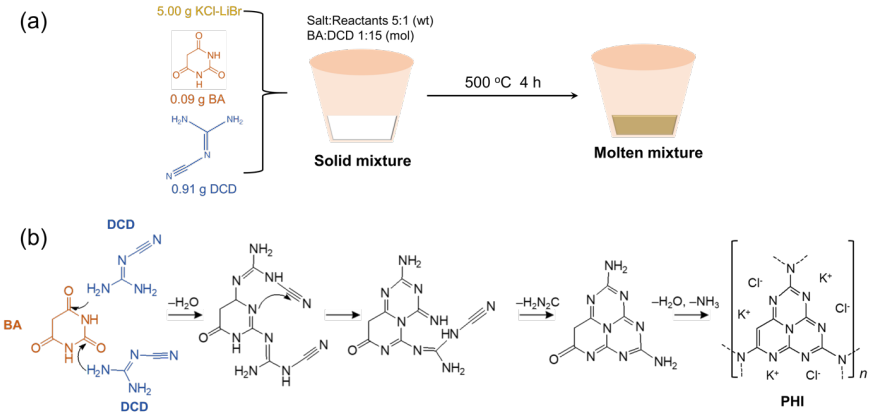

Scheme 1. (a) Synthetic procedure for DCDBA*x* synthesis. (b) Proposed mechanism for the thermal copolymerization of dicyandiamide (DCD) with barbituric acid (BA) in the presence of KCl. (Adapted from ref [35])

All the samples display XRD signals at 2θ of about 27° and 12°, which correspond to the (002) and (100) planes of CN, respectively (**Figure 1**a); a small shift occurs as the relative salt amount is increased, which can be ascribed to the intercalation of salt ions within the CN structure.[20,47] Additionally, a diffraction signal is present at approximately 8°, whose intensity is maximal for DCDBA5 and decreases at higher salt:reactants ratios; this peak can be assigned to the (100) plane of PHI structures and corresponds to a spacing distance $d_{(100)}$ of approximately 1.1 nm.[3,48] In the case of DCDBA20, however, the XRD pattern shows the formation of a crystalline PTI structure with 2θ values (10.6°, 18.4°, 22.9°, 24.7°, 26.6°, 28.0°, and 31.0°) that are slightly different from those commonly reported for PTI/Li^+Cl^-;[49–51] we ascribe this variation to the use of different salt ions in this work.

Fourier-transform infrared spectroscopy (FTIR) analysis (**Figure 1**b) provides further evidence for t polymeric carbon nitride structures formation: all materials exhibit vibration bands at 806, 1200–1700, and 2900–3500 cm^{-1}, which can be assigned to the breathing vibration of the triazine group, stretching vibrations of carbon nitride heterocyclic units, and N–H vibrational modes, respectively. In addition to these, DCDBA5 and DCDBA10 show two clear bands ca. 987 and 1605 cm^{-1}, which we assign to metal–NC_2 groups (symmetric and asymmetric vibrations of NC_2 bonds), indicating the presence of K^+–NC_2 groups.[27]

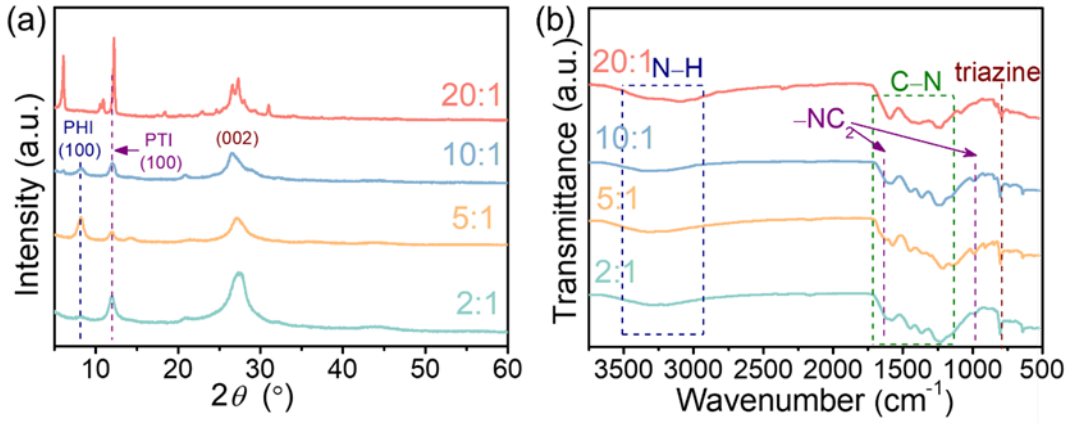

Figure 1. (a) XRD patterns and (b) FTIR spectra of DCDBA*x* powders obtained from precursors mixtures having different salt:reactants mass ratios. The patterns and spectra are vertically offset for clarity.

X-ray photoelectron spectroscopy (XPS) and organic elemental analysis (EA) provide insights into the chemical composition of the prepared CN materials. XPS survey spectra (Figure S1a–b, Table S1) show the occurrence of C, N, O, and small amounts of K and Cl; EA (Table S2) shows the presence of hydrogen from –NH moieties. The high-resolution C 1s spectra (Figure S2a–b) are deconvoluted into three peaks (284.8, 286.7, and 288.2 eV), corresponding to sp^2 carbon–carbon bonds within the structure and adventitious carbon, carbonyls, and N–C=N moieties of the triazine ring (sp^2 hybridization). The N 1s spectra (Figure S2c–d) reveal four deconvoluted peaks at binding energies of 398.6, 399.0, 400.3, and 401.2 eV, which are associated with sp^2-hybridized C–N=C within the triazine rings, N–$(C)_3$ bridging groups, N–H, and oxidized nitrogens (NO_x), respectively. The elemental content and

chemical states of DCDBA5 and DCDBA20 are almost identical, indicating the presence of similar C–N units in both.

The morphology of the different samples was examined using scanning electron microscopy (SEM, Figure S3). The powders exhibit a rod-like structure composed of small irregular particles. DCDBA20 shows a more closely packed structure and also contains some larger and more closely packed hexagonal rods than the other samples (see also Figure S4a). We focused our analysis on DCDBA5 on account of its photocatalytic activity being the highest among the samples we tested, as will be discussed later. Its morphology and crystal structure were first examined via high-resolution transmission electron microscopy (HRTEM) as shown in **Figure 2**. Two distinct lattice spacings are observed and assigned to the (100) and (002) planes of PHI ($d_{(100)}$ = 0.91–0.98 nm and $d_{(002)}$ = 0.36 nm), which correspond to the XRD peaks at 2θ of approximately 8° and 27°. However, HRTEM analysis of DCDBA20 (Figure S4) displays only one clear signal corresponding to a repeating distance of 0.36 nm, attributed to $d_{(002)}$ of PTI, and no evidence of PTI's (100) plane (lattice spacing of ca. 0.74 nm), suggesting lower in-plane order. The difference in crystallinity between the two samples does not translate into a significant difference in porosity; all samples reveal similar specific surface areas (S_A) about 130–170 $m^2\ g^{-1}$ (Brunauer–Emmet–Teller (BET) model) and a similar pore size distribution (Figure S5), which is an order of magnitude larger than that of bulk CN (10^2 vs ~10^1 $m^2\ g^{-1}$).[1]

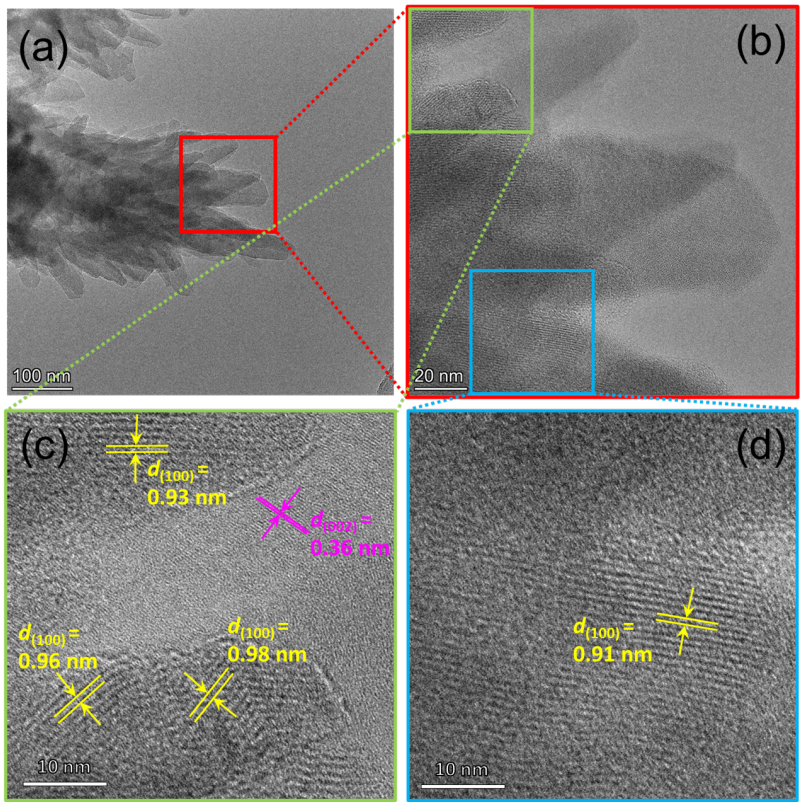

Figure 2. (a) TEM and (b–d) HRTRM images of CN from DCDBA5 (salt:reactants mass ratio of 5:1). (b) is a magnification of the square area outlined in red in (a); (c) and (d) are magnifications of the square areas outlined in green and teal in (b), respectively.

UV–vis spectroscopy shows that all the samples have an absorption edge, and the corresponding Tauc plot analyses[52] yield direct optical band gap values of 2.65, 2.75, 2.67, and 2.55 eV for DCDBA2, DCDBA5, DCDBA10, and DCDBA20, respectively (**Figure 3**a and Figure S6). By combining the optical band gap with the estimated flat band potential (obtained from Mott-Schottky analysis,[53] Figure S7), we estimated the band structure of the materials, as shown in **Figure 3**b. This analysis confirms that the conduction band (CB) shifts to more negative values when

employing higher salt:reactants ratios in the synthesis of PHI. Through the Mott-Schottky relation, we estimated charge carrier densities to be 1.9×10^{22}, 1.3×10^{22}, 1.4×10^{22}, and 2.7×10^{23} cm^{-3} for DCDBA2, DCDBA5, DCDBA10, and DCDBA20, respectively.

The assessment of the efficiency of separation of electron–hole (e^-–h^+) pairs, generated following photoexcitation, within the prepared materials, was conducted through the resultant photocurrents within a conventional photoelectrochemical cell (PEC) designed for water splitting.[15] **Figure 3**c reveals that DCDBA5 manifests the most notable photocurrent, attaining a value of ca. 10 μA cm^{-2} at 1.23 V relative to the reversible hydrogen electrode (RHE). This outcome implies that DCDBA5 has the best charge separation efficiency among the four samples. Additionally, upon examining the Nyquist plot from the electrochemical impedance spectroscopy (EIS) analysis (as depicted in Figure S8), it is evident that DCDBA5 possesses a noticeably smaller arc radius than the remaining samples. This observation confirms its lower charge transfer resistance (R_{CT}). This improvement is further supported by steady-state photoluminescence (PL) spectra (**Figure 3**d), which show a decrease in the PL intensity for DCDBA5 and DCDBA10 relative to the other samples. Fluorescence lifetime, which is the time that excited-state electrons remain in an excited state before returning to the ground state to recombine with holes, is used to reveal the separation efficiency of photogenerated e^-–h^+ pairs. DCDBA5 shows an average fluorescence lifetime τ_{DCDBA5} of 15.4 ns (obtained via time-resolved

photoluminescence decay, Figure S9 and Table S3); this value is 1.4 times as high as that of DCDBA20 (10.9 ns), suggesting a higher photogenerated charge separation rate.

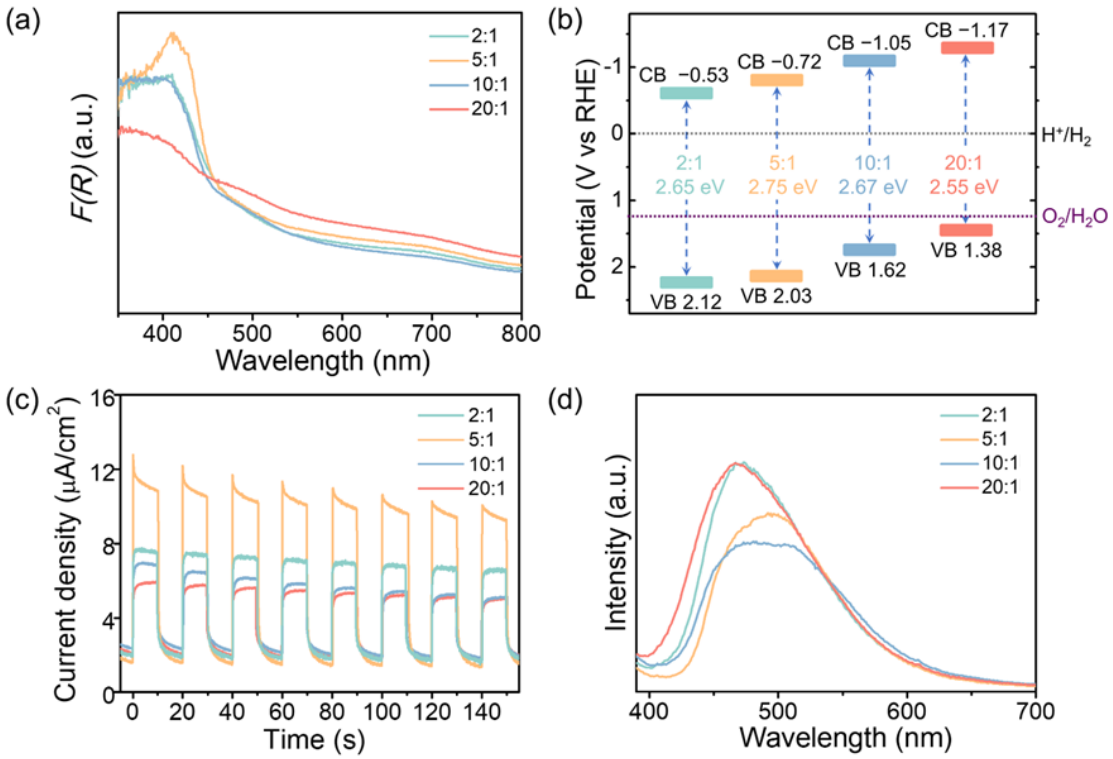

Figure 3. (a) UV–vis spectra of the powders, measured using a diffuse reflectance accessory (DRA), showing the Kubelka-Munk $F(R)$ function (proportional to absorbance). (b) Calculated energy band schemes from Tauc plots and Mott-Schottky curves, assuming that the CB minimum ≈ flat band potential. (c) Chronoamperometric photocurrent density response to on/off cycling illumination and (d) steady-state PL spectra (excitation wavelength, λ_{ex} = 370 nm) of DCDBA*x* samples.

3.2 Photocatalytic experiments

Photocatalytic HER was performed under visible light illumination ($\lambda \geq 410$ nm) for 2 h, employing a co-catalyst (Pt) and a hole scavenger (triethanolamine).[54,55] DCDBA5 showed the highest photocatalytic activity (**Figure 4**a), with a production of molecular hydrogen as high as 11449 μmol g^{-1} h^{-1} and an apparent quantum efficiency (AQE) at 405 nm of 15.6% (Figure S10). Owing to its extended optical absorption, DCDBA5 showed photocatalytic activity under illumination at longer wavelengths, with an AQE of 1.32% at 595 nm.

Even though the measured HER is a heterogeneous photocatalysis reaction occurring over a dispersed powder photoabsorber with a Pt co-catalyst, the photocatalytic hydrogen production rates of the different samples comply with the photocurrent density measurements trend and not with the specific surface area measurements one (Figure S11, data from Figure S5), nor the charge carrier density calculations (Figure S11). Therefore, we assume that the photocatalytic performance of the synthesized PHIs (DCDBA*x*) is limited by charge separation. A comparison with photocatalytic hydrogen production values from other recent CN photocatalysts reports is shown in Table S4.

To examine DCDBA5's photocatalytic stability, we reused the catalyst for four consecutive cycles (Figure S12) and showed no significant attenuation in H_2 production. The most photoactive material underwent also ORR tests to produce hydrogen peroxide in pure water under a constant O_2 flow and visible light irradiation ($\lambda \geq 410$ nm). The H_2O_2 production performance of DCDBA5 reached

66.7 μmol g^{-1} h^{-1} (i.e., 133.3 μmol L^{-1} h^{-1} , as shown in Figure S13), which is approximately a five-fold increase over bulk CN (prepared by pyrolysis of DCD for 4 h at 500 °C; 13.4 μmol g^{-1} h^{-1}); this catalyst also shows high ORR metrics relative to recent reports on photocatalytic H_2O_2 production from pure water (**Figure 4b**).[56–60]

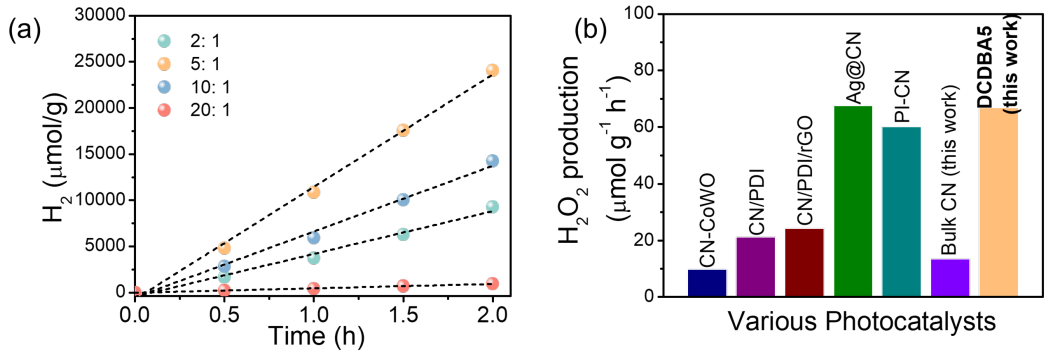

Figure 4. (a) Photocatalytic H_2 evolution over samples obtained at different salt:reactants mass ratios (DCDBA*x*). (b) Comparison chart of photocatalytic H_2O_2 production rate (normalized to catalyst mass) over different photocatalysts. Hydrogen peroxide production rates were obtained from the respective references: CN–CoWO,[56] CN/PDI,[57] CN/PDI/rGO,[58] Ag@CN,[59] and PI–CN.[60]

To explore the possibility of adapting the reported synthetic approach to a wider variety of precursors, we replaced BA with 2,4,6-triaminopyrimidine (TAP), another organic monomer also employed to increase the C-to-N ratio in synthesized CN materials, thus altering their electronic structure by the insertion of carbon atoms.[61,62] The materials were prepared by pyrolyzing mixtures of TAP and DCD at 500 °C for

4 h using different salt:reactants mass ratios. The XRD patterns and FTIR spectra of these samples resemble those of the materials prepared from BA and DCD as the precursors (see further discussion shown in Figure S14). Further SEM, optical, electrochemical, and photocatalytic characterizations are presented in Figure S15–S18. The sample prepared by employing a salt:reactants mass ratio of 10:1 (DCDTAP10) displays the strongest XRD (100) plane intensity and by far the highest photocatalytic HER activity, reaching 8474 μmol g^{-1} h^{-1}.

Remarkably, in the absence of a eutectic medium during calcination of the DCD and BA mixture or when performing an ionothermal pyrolysis using only DCD as the precursor, no XRD peaks corresponding to the (100) plane of PHI were observed (Figure S19 and S20), and the performance of the obtained CN materials was substantially lower (Figure S19b, 250 μmol g^{-1} h^{-1}). Therefore, the formation of PHI materials with significant amounts of (100) planes is attributed to the synergistic effect of the eutectic salt medium and the the two precursors' nature.

We prepared CN materials from precursor mixtures with various BA (or TAP)-to-DCD molar ratios (namely 1:30, 1:15, and 1:10 mol% of BA or TAP relative to DCD) to study the correlation between chemical composition and photocatalytic performance. The CN prepared with a BA:DCD ratio of 1:15 exhibits the highest photocatalytic hydrogen evolution activity (Figure S21b), which correlates well with its XRD pattern having the strongest intensity for the (100) plane diffraction (located at $2\theta = 8°$, Figure S20a). Similarly, the sample prepared with a TAP:DCD ratio of

1:15 shows the strongest relative diffraction intensity at 8° (XRD in Figure S22a) among all prepared DCDTAP10 materials, and its photocatalytic HER is the highest (Figure S22b).

3.3 Photocatalytic activity–crystal structure correlations

As observed, the reported PHI-based materials that display high visible-light photocatalytic activities have significantly stronger (100) plane intensity in their XRD patterns compared to other samples in this work and other reported works.[27,48,50] The intensity ratio of the diffraction peaks at 8° and 27° may be used to determine the proportion of (100) planes with repeating order within the PHI moiety, since the different CN samples (including bulk CN, PTI, or PHI) display a similar peak at approximately 27°, which is related to the interlayer stacking, that is, the (002) plane.[1,3,20,47,48] The HER activity metric and the XRD intensity ratio $I_{(100)}/I_{(002)}$ measured in different CNs (**Figure 5**a) show a direct correlation, with an excellent linear fit (R^2 = 0.918, Figure S23). Therefore, we conclude that the photocatalytic activity is linked to the in-plane crystallinity of PHI and may stem from photogenerated carriers migrating faster in-plane than between the layers—in the (002) direction.

To further understand the impact of the crystal plane on the photocatalytic processes of the synthesized PHI materials, we investigated the electronic structures of the (100) and (002) planes of different model CN structures—melon-based bulk

CN (BCN), PTI, and PHI using density functional theory (DFT) calculations. The (100) and (002) planes of BCN, PTI, and PHI were built for the calculations (Figure S24). It was shown that carrier mobility is faster in-plane than between layers in CN.[25] According to DFT calculations (Table S5), the effective electron mass (m_e*) between layers is about twice as high as the in-plane m_e* in bulk CN and PTI. However, the effective m_e* between layers is about seven times higher than the in-plane one in PHI, which indicates that the anisotropy of electron mobility is more pronounced in the PHI structure. Thus, the PHI structure, which contains a greater proportion of ordered in-plane structures, shows a higher mobility rate of electrons. These results confirm that the good photocatalytic performance of the PHIs with a higher relative abundance of ordered (100) planes can be attributed to enhancement of in-plane electron mobility (**Figure 5**b).

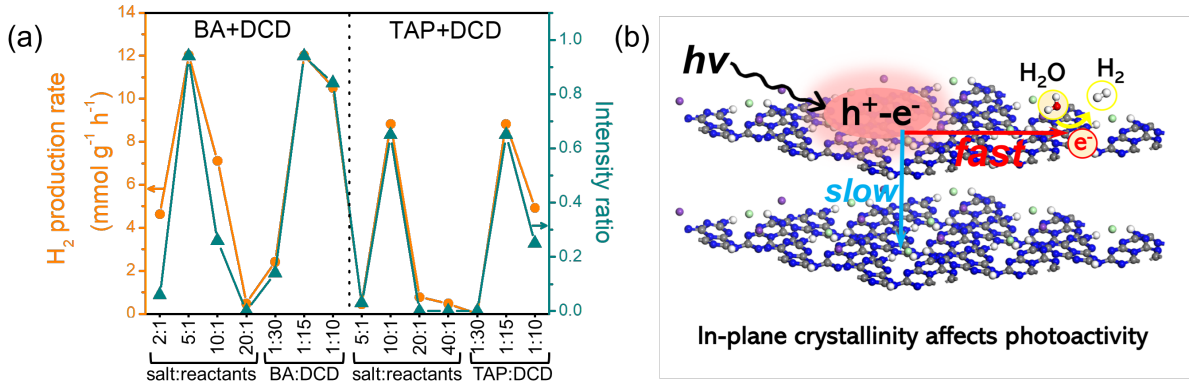

Figure 5. (a) Photocatalytic HER activity and XRD intensity ratios between $2\theta = 8°$ and $2\theta = 27°$, $I_{(100)}/I_{(002)}$, for PHI CN samples obtained under different conditions. The samples were prepared from mixtures of DCD and BA (left) or TAP (right). Using DCD and BA as precursors, samples were prepared using various salt:reactants mass ratios (BA:DCD mole ratio fixed at 1:15) and various BA:DCD

ratios (salt:reactants mass ratio fixed at 5:1). Similarly, using DCD and TAP as precursors, samples were prepared using various salt:reactants mass ratios (TAP:DCD mole ratio fixed at 1:15) and various BA:DCD ratios (fixed salt:reactants mass ratio at 10:1). (b) Scheme of photocatalytic activity enhancement mechanism through fast in-plane (100) electron migration.

4. CONCLUSIONS

In summary, in this work, we correlated the photocatalytic activity of crystalline PHI materials to their crystal structure. By co-polymerizing different CN-based organic molecules in a salt medium at different salt:reactants mass ratios, we prepared a set of crystalline CN materials with different proportions of PHI (100) planes. The materials with a higher abundance of PHI (100) planes exhibited the best performance towards photocatalytic production of H_2O_2 in pure water under visible light (66.7 μmol g^{-1} h^{-1}). The most photoactive material showed apparent quantum efficiencies for the photocatalytic hydrogen evolution reaction of 15.6% at 405 nm and 1.32% at 595 nm. We identified that the reported materials' photocatalytic activity is linearly correlated with the (100)-to-(002) X-ray diffraction intensities ratio. Furthermore, DFT calculations confirm that the high photocatalytic performance of PHI rich in ordered (100) planes arises from enhanced in-plane electron mobility. We believe that the novel PHI-based materials prepared in this work and the implications arising from the activity–crystal structure correlations will open new avenues for photocatalysts design.

ASSOCIATED CONTENT

Supporting Information: The Supporting Information is available free of charge at https://pubs.acs.org/doi/10.1021/acs.energyfuels.XXX.

Detailed experimental details, further characterization and photocatalysis analyses (PDF).

AUTHOR INFORMATION

Corresponding Author

Jesús Barrio, Department of Chemical Engineering, Imperial College London, Royal School of Mines, London SW72AZ, England, UK. E-mail: j.barrio-hermida@imperial.ac.uk

Menny Shalom, Department of Chemistry and Ilse Katz Institute for Nanoscale Science and Technology, Ben-Gurion University of the Negev, Beer-Sheva 8410501, Israel. E-mail: mennysh@bgu.ac.il

Xirui Zhang, State Key Laboratory of Photocatalysis on Energy and Environment, College of Chemistry, Fuzhou University, Fuzhou, 350116 P. R. China. E-mail: dardons@126.com

Author Contributions

The manuscript was written through contributions of all authors. All authors have given approval to the final version of the manuscript.

Notes

There are no conflicts to declare.

ACKNOWLEDENMENTS

This work was financially supported by the Israel Science Foundation (ISF) Grant No. 601/21 and ISF-NSFC Grant No. 2969/19. This project has received funding from the European Research Council (ERC) under the European Union's Horizon 2020 research and innovation programme (Grant Agreement No. 849068). Junyi Li thanks the China Scholarships Council for its financial support.

REFERENCES

(1) Wang, X.; Maeda, K.; Thomas, A.; Takanabe, K.; Xin, G.; Carlsson, J. M.; Domen, K.; Antonietti, M. A Metal-Free Polymeric Photocatalyst for Hydrogen Production from Water under Visible Light. *Nat Mater* **2009**, *8* (1), 76–80. https://doi.org/10.1038/nmat2317.

(2) Kessler, F. K.; Zheng, Y.; Schwarz, D.; Merschjann, C.; Schnick, W.; Wang, X.; Bojdys, M. J. Functional Carbon Nitride Materials — Design Strategies for Electrochemical Devices. *Nat Rev Mater* **2017**, *2* (6), 17030. https://doi.org/10.1038/natrevmats.2017.30.

(3) Lin, L.; Yu, Z.; Wang, X. Crystalline Carbon Nitride Semiconductors for Photocatalytic Water Splitting. *Angewandte Chemie International Edition* **2019**, *58* (19), 6164–6175. https://doi.org/10.1002/anie.201809897.

(4) Ong, W. J.; Tan, L. L.; Ng, Y. H.; Yong, S. T.; Chai, S. P. Graphitic Carbon Nitride (g-C3N4)-Based Photocatalysts for Artificial Photosynthesis and Environmental Remediation: Are We a Step Closer to Achieving Sustainability? *Chem Rev* **2016**, *116* (12), 7159–7329. https://doi.org/10.1021/acs.chemrev.6b00075.

(5) Barrio, J.; Volokh, M.; Shalom, M. Polymeric Carbon Nitrides and Related Metal-Free Materials for Energy and Environmental Applications. *J Mater Chem A Mater* **2020**, *8* (22), 11075–11116.

https://doi.org/10.1039/d0ta01973a.

(6) Li, Y.; Li, B.; Zhang, D.; Cheng, L.; Xiang, Q. Crystalline Carbon Nitride Supported Copper Single Atoms for Photocatalytic CO2Reduction with Nearly 100% CO Selectivity. *ACS Nano* **2020**, *14* (8), 10552–10561. https://doi.org/10.1021/acsnano.0c04544.

(7) Lin, J.; Pan, Z.; Wang, X. Photochemical Reduction of CO 2 by Graphitic Carbon Nitride Polymers. *ACS Sustain Chem Eng* **2014**, *2*, 353–358. https://doi.org/10.1021/sc4004295.

(8) Barrio, J.; Mateo, D.; Albero, J.; García, H.; Shalom, M. A Heterogeneous Carbon Nitride–Nickel Photocatalyst for Efficient Low-Temperature CO 2 Methanation. *Adv Energy Mater* **2019**, *9* (44), 1902738. https://doi.org/10.1002/aenm.201902738.

(9) Yan, B.; Chen, Z.; Xu, Y. Amorphous and Crystalline 2D Polymeric Carbon Nitride Nanosheets for Photocatalytic Hydrogen/Oxygen Evolution and Hydrogen Peroxide Production. *Chemistry - An Asian Journal*. 2020, pp 2329–2340. https://doi.org/10.1002/asia.202000253.

(10) Hu, J.; Chen, C.; Yang, H.; Yang, F.; Qu, J.; Yang, X.; Sun, W.; Dai, L.; Li, C. M. Tailoring Well-Ordered, Highly Crystalline Carbon Nitride Nanoarrays via Molecular Engineering for Efficient Photosynthesis of H2O2. *Appl Catal B* **2022**, *317*, 121723. https://doi.org/10.1016/j.apcatb.2022.121723.

(11) Yang, Z.; Li, L.; Zeng, S.; Cui, J.; Wang, K.; Hu, C.; Zhao, Y. Nanoarchitecture Manipulation by Polycondensation on KCl Crystals toward Crystalline Lamellar Carbon Nitride for Efficient H2O2 Photoproduction. *ACS Appl Mater Interfaces* **2022**, *15* (6), 8232–8240. https://doi.org/10.1021/acsami.2c22366.

(12) Mazzanti, S.; Savateev, A. Emerging Concepts in Carbon Nitride Organic Photocatalysis. *Chempluschem* **2020**, *85* (11), 2499–2517. https://doi.org/https://doi.org/10.1002/cplu.202000606.

(13) Mazzanti, S.; Kurpil, B.; Pieber, B.; Antonietti, M.; Savateev, A. Dichloromethylation of Enones by Carbon Nitride Photocatalysis. *Nat Commun* **2020**, *11* (1), 1387. https://doi.org/10.1038/s41467-020-15131-0.

(14) Savateev, A.; Antonietti, M. Heterogeneous Organocatalysis for Photoredox Chemistry. *ACS Catal* **2018**, *8* (10), 9790–9808. https://doi.org/10.1021/acscatal.8b02595.

(15) Volokh Menny Shalom, M.; Volokh, M. Polymeric Carbon Nitride as a Platform for Photoelectrochemical Water-Splitting Cells. *Ann NY Acad Sci* **2023**, 1–9. https://doi.org/10.1111/nyas.14963.

(16) Li, H.; Wang, C.; Bai, X.; Wang, X.; Sun, B.; Li, D.; Zhao, L.; Zong, R.; Hao, D. In-Plane Polarization Induced by the Hydrogen Bonding and π–π Stacking of Functionalized PDI Supramolecules for the Efficient Photocatalytic Degradation of Organic Pollutants. *Mater Chem Front* **2020**, *4* (9), 2673–2687. https://doi.org/10.1039/D0QM00349B.

(17) Bai, X.; Jia, T.; Wang, X.; Hou, S.; Hao, D.; Bingjie-Ni. High Carrier Separation Efficiency for a Defective G-C $_3$ N $_4$ with Polarization Effect and Defect Engineering: Mechanism, Properties and Prospects. *Catal Sci Technol* **2021**, *11* (16), 5432–5447. https://doi.org/10.1039/D1CY00595B.

(18) Bai, X.; Jia, T.; Hao, D.; Xin, Y.; Guo, L. Tremendous Boost in the Photocatalytic Properties of G-C_3N_4 : Regulation from Polymerization Kinetics to Crystal Structure Engineering.

CrystEngComm **2022**, *24* (11), 2023–2035. https://doi.org/10.1039/D1CE01547H.

(19) Lin, L.; Wang, C.; Ren, W.; Ou, H.; Zhang, Y.; Wang, X. Photocatalytic Overall Water Splitting by Conjugated Semiconductors with Crystalline Poly(Triazine Imide) Frameworks. *Chem Sci* **2017**, *8* (8), 5506–5511. https://doi.org/10.1039/c7sc00900c.

(20) Bojdys, M. J.; Müller, J. O.; Antonietti, M.; Thomas, A. Ionothermal Synthesis of Crystalline, Condensed, Graphitic Carbon Nitride. *Chemistry - A European Journal* **2008**, *14* (27), 8177–8182. https://doi.org/10.1002/chem.200800190.

(21) Burmeister, D.; Müller, J.; Plaickner, J.; Kochovski, Z.; List-Kratochvil, E. J. W.; Bojdys, M. J. Size Effects of the Anions in the Ionothermal Synthesis of Carbon Nitride Materials. *Chemistry - A European Journal* **2022**, *28* (33), e202200705. https://doi.org/10.1002/chem.202200705.

(22) Dontsova, D.; Pronkin, S.; Wehle, M.; Chen, Z.; Fettkenhauer, C.; Clavel, G.; Antonietti, M. Triazoles: A New Class of Precursors for the Synthesis of Negatively Charged Carbon Nitride Derivatives. *Chemistry of Materials* **2015**, *27* (15), 5170–5179. https://doi.org/10.1021/acs.chemmater.5b00812.

(23) Savateev, A.; Pronkin, S.; Epping, J. D.; Willinger, M. G.; Wolff, C.; Neher, D.; Antonietti, M.; Dontsova, D. Potassium Poly(Heptazine Imides) from Aminotetrazoles: Shifting Band Gaps of Carbon Nitride-like Materials for More Efficient Solar Hydrogen and Oxygen Evolution. *ChemCatChem* **2017**, *9* (1), 167–174. https://doi.org/10.1002/cctc.201601165.

(24) Savateev, A.; Pronkin, S.; Willinger, M. G.; Antonietti, M.; Dontsova, D. Towards Organic Zeolites and Inclusion Catalysts: Heptazine Imide Salts Can Exchange Metal Cations in the Solid State. *Chem Asian J* **2017**, *12* (13), 1517–1522. https://doi.org/10.1002/asia.201700209.

(25) Lin, L.; Lin, Z.; Zhang, J.; Cai, X.; Lin, W.; Yu, Z.; Wang, X. Molecular-Level Insights on the Reactive Facet of Carbon Nitride Single Crystals Photocatalysing Overall Water Splitting. *Nat Catal* **2020**, *3* (8), 649–655. https://doi.org/10.1038/s41929-020-0476-3.

(26) Lin, L.; Ou, H.; Zhang, Y.; Wang, X. Tri-s-Triazine-Based Crystalline Graphitic Carbon Nitrides for Highly Efficient Hydrogen Evolution Photocatalysis. *ACS Catal* **2016**, *6* (6), 3921–3931. https://doi.org/10.1021/acscatal.6b00922.

(27) Zhang, G.; Li, G.; Lan, Z. A.; Lin, L.; Savateev, A.; Heil, T.; Zafeiratos, S.; Wang, X.; Antonietti, M. Optimizing Optical Absorption, Exciton Dissociation, and Charge Transfer of a Polymeric Carbon Nitride with Ultrahigh Solar Hydrogen Production Activity. *Angewandte Chemie - International Edition* **2017**, *56* (43), 13445–13449. https://doi.org/10.1002/anie.201706870.

(28) Zhang, H.; Cao, Y.; Li, Z.; Gao, Y.; Shangguan, L.; Sun, J.; Lang, L.; Lei, W. Improved Charge Transport through 2D Framework in Fully Condensed Carbon Nitride for Efficient Photocatalytic Hydrogen Production. *J Catal* **2023**, 417, 360–367. https://doi.org/https://doi.org/10.1016/j.jcat.2022.12.018.

(29) Lau, V. W.; Yu, V. W.; Ehrat, F.; Botari, T.; Moudrakovski, I.; Simon, T.; Duppel, V.; Medina, E.; Stolarczyk, J. K.; Feldmann, J.; Blum, V.; Lotsch, B. V. Urea-Modified Carbon Nitrides: Enhancing Photocatalytic Hydrogen Evolution by Rational Defect Engineering. *Adv Energy Mater* **2017**, *7* (12), 1602251. https://doi.org/10.1002/aenm.201602251.

(30) Lau, V. W.; Moudrakovski, I.; Botari, T.; Weinberger, S.; Mesch, M. B.; Duppel, V.; Senker, J.; Blum, V.; Lotsch, B. V. Rational Design of Carbon Nitride Photocatalysts by Identification of

Cyanamide Defects as Catalytically Relevant Sites. *Nat Commun* **2016**, *7* (1), 12165. https://doi.org/10.1038/ncomms12165.

(31) Teixeira, I. F.; Tarakina, N. V; Silva, I. F.; Atta Diab, G. A.; Salas, N. L.; Savateev, A.; Antonietti, M. Improving Hydrogen Production for Carbon-Nitride-Based Materials: Crystallinity, Cyanimide Groups and Alkali Metals in Solution Working Synergistically. *J Mater Chem A Mater* **2022**, *10* (35), 18156–18161. https://doi.org/10.1039/D2TA05571F.

(32) Barrio, J.; Barzilai, S.; Karjule, N.; Amo-Ochoa, P.; Zamora, F.; Shalom, M. Synergistic Doping and Surface Decoration of Carbon Nitride Macrostructures by Single Crystal Design. *ACS Appl Energy Mater* **2021**, *4* (2), 1868–1875. https://doi.org/10.1021/acsaem.0c02964.

(33) Li, X.; Bartlett, S. A.; Hook, J. M.; Sergeyev, I.; Clatworthy, E. B.; Masters, A. F.; Maschmeyer, T. Salt-Enhanced Photocatalytic Hydrogen Production from Water with Carbon Nitride Nanorod Photocatalysts: Cation and PH Dependence. *J Mater Chem A Mater* **2019**, *7* (32), 18987–18995. https://doi.org/10.1039/C9TA04942H.

(34) Teixeira, I. F.; Tarakina, N. V; Silva, I. F.; López-Salas, N.; Savateev, A.; Antonietti, M. Overcoming Electron Transfer Efficiency Bottlenecks for Hydrogen Production in Highly Crystalline Carbon Nitride-Based Materials. *Adv Sustain Syst* **2022**, *6* (3), 2100429. https://doi.org/https://doi.org/10.1002/adsu.202100429.

(35) Zhang, J.; Chen, X.; Takanabe, K.; Maeda, K.; Domen, K.; Epping, J. D.; Fu, X.; Antonieta, M.; Wang, X. Synthesis of a Carbon Nitride Structure for Visible-Light Catalysis by Copolymerization. *Angewandte Chemie - International Edition* **2010**, *49* (2), 441–444. https://doi.org/10.1002/anie.200903886.

(36) Ho, W.; Zhang, Z.; Lin, W.; Huang, S.; Zhang, X.; Wang, X.; Huang, Y. Copolymerization with 2,4,6-Triaminopyrimidine for the Rolling-up the Layer Structure, Tunable Electronic Properties, and Photocatalysis of g-C3N4. *ACS Appl Mater Interfaces* **2015**, *7* (9), 5497–5505. https://doi.org/10.1021/am509213x.

(37) Kröger, J.; Jiménez-Solano, A.; Savasci, G.; Rovó, P.; Moudrakovski, I.; Küster, K.; Schlomberg, H.; Vignolo-González, H. A.; Duppel, V.; Grunenberg, L.; Dayan, C. B.; Sitti, M.; Podjaski, F.; Ochsenfeld, C.; Lotsch, B. V. Interfacial Engineering for Improved Photocatalysis in a Charge Storing 2D Carbon Nitride: Melamine Functionalized Poly(Heptazine Imide). *Adv Energy Mater* **2021**, *11* (6), 2003016. https://doi.org/10.1002/aenm.202003016.

(38) Barrio, J.; Barzilai, S.; Karjule, N.; Amo-Ochoa, P.; Zamora, F.; Shalom, M. Synergistic Doping and Surface Decoration of Carbon Nitride Macrostructures by Single Crystal Design. *ACS Appl Energy Mater* **2021**, *4* (2), 1868–1875. https://doi.org/10.1021/acsaem.0c02964.

(39) Zhao, X.; You, Y.; Huang, S.; Wu, Y.; Ma, Y.; Zhang, G.; Zhang, Z. Z-scheme Photocatalytic Production of Hydrogen Peroxide over Bi4O5Br2/g-C3N4 Heterostructure under Visible Light. *Appl Catal B* **2020**, *278*, 119251. https://doi.org/10.1016/j.apcatb.2020.119251.

(40) Zheng, Y.; Yu, Z.; Ou, H.; Asiri, A. M.; Chen, Y.; Wang, X. Black Phosphorus and Polymeric Carbon Nitride Heterostructure for Photoinduced Molecular Oxygen Activation. *Adv Funct Mater* **2018**, *28* (10), 1705407. https://doi.org/10.1002/adfm.201705407.

(41) Kresse, G.; Hafner, J. Ab Initio Molecular-Dynamics Simulation of the Liquid-Metalamorphous- Semiconductor Transition in Germanium. *Phys Rev B* **1994**, *49* (20), 14251–

14269. https://doi.org/10.1103/PhysRevB.49.14251.

(42) Blöchl, P. E. Projector Augmented-Wave Method. *Phys Rev B* **1994**, *50* (24), 17953–17979. https://doi.org/10.1103/PhysRevB.50.17953.

(43) Perdew, J. P.; Burke, K.; Ernzerhof, M. Generalized Gradient Approximation Made Simple. *Phys Rev Lett* **1996**, *77* (18), 3865–3868. https://doi.org/10.1103/PhysRevLett.77.3865.

(44) Perdew, J. P.; Ernzerhof, M.; Burke, K. Rationale for Mixing Exact Exchange with Density Functional Approximations. *Journal of Chemical Physics* **1996**, *105* (22), 9982–9985. https://doi.org/10.1063/1.472933.

(45) Grimme, S.; Antony, J.; Ehrlich, S.; Krieg, H. A Consistent and Accurate *Ab Initio* Parametrization of Density Functional Dispersion Correction (DFT-D) for the 94 Elements H-Pu. *J Chem Phys* **2010**, *132* (15), 154104. https://doi.org/10.1063/1.3382344.

(46) Li, J.; Wang, X.; Huang, L.; Tian, L.; Shalom, M.; Xiong, C.; Zhang, H.; Jia, Q.; Zhang, S.; Liang, F. Ultrathin Mesoporous Graphitic Carbon Nitride Nanosheets with Functional Cyano Group Decoration and Nitrogen-Vacancy Defects for an Efficient Selective CO2photoreduction. *Nanoscale* **2021**, *13* (29), 12634–12641. https://doi.org/10.1039/d1nr02639a.

(47) Tian, L.; Li, J.; Liang, F.; Wang, J.; Li, S.; Zhang, H.; Zhang, S. Molten Salt Synthesis of Tetragonal Carbon Nitride Hollow Tubes and Their Application for Removal of Pollutants from Wastewater. *Appl Catal B* **2018**, *225*, 307–313. https://doi.org/10.1016/j.apcatb.2017.11.082.

(48) Liu, G.; Tang, Z.; Gu, X.; Li, N.; Lv, H.; Huang, Y. Boosting Photocatalytic Nitrogen Reduction to Ammonia by Dual Defective – N and K-Doping Sites on Graphitic Carbon Nitride Nanorod Arrays. *Appl Catal B* **2022**, *317*, 121752. https://doi.org/10.1016/j.apcatb.2022.121752.

(49) Chong, S. Y.; Jones, J. T. A.; Khimyak, Y. Z.; Cooper, A. I.; Thomas, A.; Antonietti, M.; Bojdys, M. J. Tuning of Gallery Heights in a Crystalline 2D Carbon Nitride Network. *J Mater Chem A Mater* **2013**, *1* (4), 1102–1107. https://doi.org/10.1039/c2ta01068b.

(50) Sun, Z.; Dong, H.; Yuan, Q.; Tan, Y.; Wang, W.; Jiang, Y.; Wan, J.; Wen, J.; Yang, J.; He, J.; Cheng, T.; Huang, L. Self-Supported Hierarchical Crystalline Carbon Nitride Arrays with Triazine-Heptazine Heterojunctions for Highly Efficient Photoredox Catalysis. *Chemical Engineering Journal* **2022**, *435*, 134865. https://doi.org/10.1016/j.cej.2022.134865.

(51) Chen, Z.; Savateev, A.; Pronkin, S.; Papaefthimiou, V.; Wolff, C.; Willinger, M. G.; Willinger, E.; Neher, D.; Antonietti, M.; Dontsova, D. "The Easier the Better" Preparation of Efficient Photocatalysts—Metastable Poly(Heptazine Imide) Salts. *Advanced Materials* **2017**, *29* (32), 1–8. https://doi.org/10.1002/adma.201700555.

(52) Makuła, P.; Pacia, M.; Macyk, W. How To Correctly Determine the Band Gap Energy of Modified Semiconductor Photocatalysts Based on UV–Vis Spectra. *J Phys Chem Lett* **2018**, *9* (23), 6814–6817. https://doi.org/10.1021/acs.jpclett.8b02892.

(53) Hankin, A.; Bedoya-Lora, F. E.; Alexander, J. C.; Regoutz, A.; Kelsall, G. H. Flat Band Potential Determination: Avoiding the Pitfalls. *J Mater Chem A Mater* **2019**, *7* (45), 26162–26176. https://doi.org/10.1039/C9TA09569A.

(54) Xia, J.; Karjule, N.; Mark, G.; Volokh, M.; Chen, H.; Shalom, M. Aromatic Alcohols Oxidation and Hydrogen Evolution over π-Electron Conjugated Porous Carbon Nitride Rods. *Nano Res* **2022**, *15* (12), 10148–10157. https://doi.org/10.1007/s12274-022-4717-4.

(55) Mark, G.; Mondal, S.; Volokh, M.; Xia, J.; Shalom, M. Halogen–Hydrogen Bonding for the Synthesis of Efficient Polymeric Carbon-Nitride Photocatalysts. *Solar RRL* **2022**, *6* (12), 2200834. https://doi.org/10.1002/solr.202200834.

(56) Zhao, S.; Zhao, X. Insights into the Role of Singlet Oxygen in the Photocatalytic Hydrogen Peroxide Production over Polyoxometalates-Derived Metal Oxides Incorporated into Graphitic Carbon Nitride Framework. *Appl Catal B* **2019**, *250*, 408–418. https://doi.org/10.1016/j.apcatb.2019.02.031.

(57) Shiraishi, Y.; Kanazawa, S.; Kofuji, Y.; Sakamoto, H.; Ichikawa, S.; Tanaka, S.; Hirai, T. Sunlight-Driven Hydrogen Peroxide Production from Water and Molecular Oxygen by Metal-Free Photocatalysts. *Angewandte Chemie - International Edition* **2014**, *53* (49), 13454–13459. https://doi.org/10.1002/anie.201407938.

(58) Kofuji, Y.; Isobe, Y.; Shiraishi, Y.; Sakamoto, H.; Tanaka, S.; Ichikawa, S.; Hirai, T. Carbon Nitride-Aromatic Diimide-Graphene Nanohybrids: Metal-Free Photocatalysts for Solar-to-Hydrogen Peroxide Energy Conversion with 0.2% Efficiency. *J Am Chem Soc* **2016**, *138* (31), 10019–10025. https://doi.org/10.1021/jacs.6b05806.

(59) Cai, J.; Huang, J.; Wang, S.; Iocozzia, J.; Sun, Z.; Sun, J.; Yang, Y.; Lai, Y.; Lin, Z. Crafting Mussel-Inspired Metal Nanoparticle-Decorated Ultrathin Graphitic Carbon Nitride for the Degradation of Chemical Pollutants and Production of Chemical Resources. *Advanced Materials* **2019**, *31* (15), 1806314. https://doi.org/10.1002/adma.201806314.

(60) Yang, L.; Dong, G.; Jacobs, D. L.; Wang, Y.; Zang, L.; Wang, C. Two-Channel Photocatalytic Production of H2O2 over g-C3N4 Nanosheets Modified with Perylene Imides. *J Catal* **2017**, *352*, 274–281. https://doi.org/10.1016/j.jcat.2017.05.010.

(61) Li, J.; Karjule, N.; Qin, J.; Wang, Y.; Barrio, J.; Shalom, M. Low-Temperature Synthesis of Solution Processable Carbon Nitride Polymers. *Molecules* **2021**, *26* (6), 1646. https://doi.org/10.3390/molecules26061646.

(62) Li, J.; Dor, S.; Barrio, J.; Shalom, M. Efficient Water Cleaning by Self-Standing Carbon Nitride Films Derived from Supramolecular Hydrogels. *Chemistry – A European Journal* **2022**, *28* (58), e202201969. https://doi.org/https://doi.org/10.1002/chem.202201969.

TOC Graphic

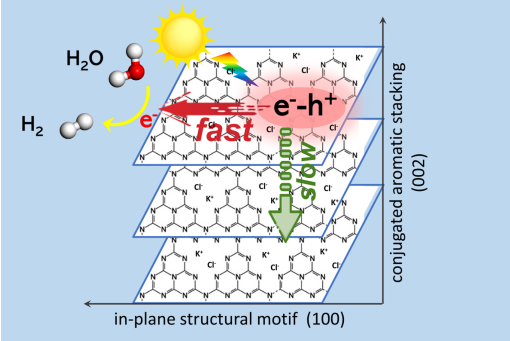
H2O
H2
e-
fast
e-h+
slow
conjugated aromatic stacking
(002)
in-plane structural motif (100)

Supporting Information

Elucidating the Effect of Crystallinity on Photoactivity in Poly(heptazine imides)

Junyi Li,[a] Jesús Barrio,[b] Yuanxing Fang,[c] Yongxin Pan,[c] Michael Volokh,[a] Sanjit Mondal,[a] Jonathan Tzadikov,[a] Liel Abisdris,[a] Ayelet Tashakory,[a] Xinchen Wang,[c] Xirui Zhang*[c] and Menny Shalom*[a]*

a. Department of Chemistry and Ilse Katz Institute for Nanoscale Science and Technology, Ben-Gurion University of the Negev, Beer-Sheva 8410501, Israel. E-mail: mennysh@bgu.ac.il

b. Department of Chemical Engineering, Imperial College London, Royal School of Mines, London SW72AZ, England, UK. E-mail: j.barrio-hermida@imperial.ac.uk

c. State Key Laboratory of Photocatalysis on Energy and Environment, College of Chemistry, Fuzhou University, Fuzhou, 350116 P. R. China. E-mail: dardons@126.com

Materials and Characterization

1. Materials

All chemicals were purchased from the specified commercial suppliers and employed in their original forms (see purity for each material). Deionized (DI) water, used for all aqueous solution preperation, was obtained via a Millipore Direct-Q system (with a room temperature resistivity of 18.2 MΩ cm). Dicyandiamide (DCD, 99%), chloroplatinic acid solution (8 wt.% H_2PtCl_6 in H_2O), barbituric acid (BA, 99%), potassium chloride (KCl, 99%), potassium permanganate ($KMnO_4$, 99%), and 2,4,6-triaminopyrimidine (TAP, 97%) were obtained from Sigma-Aldrich; lithium bromide (LiBr, 99%) from Glentham, UK; triethanolamine (TEOA, 99%) from Carl Roth; KOH (85%) and Na_2SO_4 (99%) from Loba-Chemie, India; hydrogen peroxide (H_2O_2, 30 wt.%) from J. T. Baker; sulfuric acid (H_2SO_4, 96 wt.%) from Carlo Erba. Fluorine-doped tin oxide (FTO)-coated glass (TEC 15; 12–14 Ω sq^{-1}) was purchased from Xop Glass, Spain. Prior to utilization, the FTO glass underwent an extensive cleansing process involving sequential washing with an aqueous solution of a detergent (Alconox, ca. 1 wt.% aqueous solution), followed by acetone and ethanol, after which they were subjected to drying at a temperature of 60 °C.

2. Characterization

Fourier-transform infrared spectroscopy (FTIR) was measured by a Thermo Scientific Nicolet iS5 (KBr window, diamond iD7 ATR optical base). X-ray diffraction (XRD) patterns were obtained using an Empyrean powder diffractometer (Panalytical, position-sensitive detector X'Celerator, operation parameters: Cu Kα, λ = 1.54178 Å, 40 kV, 30 mA) with a scanning range of 2θ between 5° and 60°). Scanning electron microscopy (SEM) was used to characterize the morphology of the materials (FEI Verios 460 L equipped with a FEG source operated at U_0 = 3.5 kV; before analysis, the samples were coated via sputtering with approximately 12 nm

Au to enhance conductivity and minimize charging effects). Transmission electron microscopy (TEM) was performed on a Thermo Fisher Scientific field emission microscope (Talos F200S) operated at an acceleration voltage of 200 kV. Nitrogen sorption measurements and Brunauer–Emmet–Teller (BET) specific surface area calculations were performed on a Quantachrome NOVAtouch NT LX^3 system at 77 K. Ultraviolet–visible spectroscopy (UV–vis) spectra were recorded using a Cary 100 spectrophotometer. Photoluminescence (PL) spectra were recorded on a FluoroMax® 4 spectrofluorometer (Horiba Scientific) excited at a wavelength of 370 nm. Time-resolved fluorescence measurements were performed on a time-correlated single-photon counting (TCSPC) setup with a Horiba Fluorolog modular spectrofluorometer. The PL lifetimes (τ_{av}) were estimated from time-resolved PL spectra decay curves to which a triple-exponential function was fitted: $\tau_{av} = \sum_{i=1}^{i=3} A_i \tau_i^2 / \sum_{i=1}^{i=3} A_i \tau_i$, where τ_i is the lifetime and A_i is the amplitude of the i^{th} component; $A_1 + A_2 + A_3 = 1$. X-ray photoelectron spectroscopy (XPS) was performed on a Thermo Fisher Scientific ESCALAB 250 using monochromated Al Kα X-rays (1486.6 eV). Electrochemical measurements (including EIS) were recorded using a three-electrode system on an Autolab potentiostat (Metrohm, PGSTAT302N). The working electrode was prepared using FTO-coated glass: the catalyst (10 mg) was mixed with acetone (2 mL), and the mixture was ultrasonicated for 30 min. The slurry was cast onto a 0.25 cm^2 FTO-coated glass plate and annealed at 473 K for 30 min in air to improve adhesion. A 1 cm^2 Pt-foil electrode and an Ag/AgCl (sat. KCl) electrode were used as the counter and reference electrodes, respectively. A Newport 300 W Xe arc lamp equipped with air mass AM 1.5G and water filters was used as the light source. The intensity of the incident light (one-sun illumination) was calibrated using a Newport 919P thermopile photometer. Photocurrent measurements and electrochemical impedance spectroscopy were conducted in a 0.1 M KOH aqueous solution (pH = 13). Mott–Schottky measurements were performed in a 1.0 M Na_2SO_4 aqueous solution (pH = 7) at a frequency of 2.48 kHz.

3. Photocatalytic H_2 production

Hydrogen evolution reaction (HER) measurements were performed using a thermostatically-controlled quartz vessel and a white 100 W LED array (Bridgelux BXRA-50C5300; $\lambda \geq 410$ nm) as the irradiation source. In a typical process, 15 mg of the sample was placed inside a 50 mL quartz vessel with a solvent mixture (19 mL) composed of water and TEOA in a 9:1 (v/v) ratio, and 19.6 μL of an 8 wt.% H_2PtCl_6 solution in water (corresponding to a theoretical value of 3 wt.% Pt loading onto the catalyst, total concentration of 0.207 mM) was added; the temperature was maintained at 25 °C with a thermostat. After stirring for 30 min in the dark under a constant flow of argon, the reaction was started by switching on the LED array. Gas chromatography (Agilent 7820 GC System) was used to confirm that the evolved gas was hydrogen and to monitor the amount generated per hour after the 30 min photodeposition of Pt co-catalyst. All H_2 tests by GC were performed thrice to verify their difference was within 3%. The stability test was a continuous measurement of four sequential cycles with an argon purge of the headspace between cycles. AQE measurements were performed in a sealed reactor connected to an argon line and an Agilent 7820 GC system. Argon gas was continually flowed through the reactor in the dark to remove the existing hydrogen, nitrogen, oxygen, and other gases, and the purging process was monitored by automatic sampling every 11 min. After the purge, a Thorlabs LED (λ = 395, 405, 415, 430, 455, 490, 530, and 595 nm) was turned on, the hydrogen produced was recorded, and the integrated area was used for the calculation of the AQE was determined according to Equation (S1) assuming monochromatic illumination:

$$\mathrm{AQE} = N_e/N_p \times 100\% = 2M/N_p \times 100\% \quad \text{(S1)}$$

where N_e is the number of reaction electrons, N_p is the number of incident photons, and M is the number of H_2 molecules.

4. Photocatalytic H_2O_2 production

Photocatalytic O_2 reduction reaction (ORR) experiments to produce H_2O_2 were carried out by adding 50 mg of photocatalyst to 25 mL of deionized water in a quartz vessel (maximum diameter φ = 60 mm; capacity 100 mL). The vessel was sealed with a rubber septum cap and the reaction media was purged with O_2(g) for 30 min and subjected to ultrasonication to ensure the dispersion of the catalyst. The temperature of the reactor vessel was controlled using a 30 °C jacketed beaker connected to a circulating cooling system. The quartz vessel was irradiated using a 100 W white LED array (Bridgelux BXRA-50C5300, $\lambda \geq 410$ nm) under constant O_2 flow. The hydrogen peroxide product amount was colorimetrically determined using an aqueous potassium permanganate solution. The untested aqueous solution was centrifuged first, and 1.00 mL of the supernatant was taken to be mixed with 1.00 mL of [H_2SO_4(aq)] = 0.50 M and 1.00 mL [$KMnO_4$(aq)] = 10 mM. After standing for 30 min, UV–vis absorbance was used to quantify the H_2O_2 using the absorption peak at 524 nm after establishing a calibration curve.

Table S1. Elemental composition of DCDBA*x* samples, determined by XPS.

	N (at.%)	**C (at.%)**	**O (at.%)**	**K (at.%)**	**Cl (at.%)**
DCDBA5	49.72	45.12	2.74	2.21	0.21
DCDBA20	52.2	43.99	2.61	1.01	0.19

Table S2. Organic elemental analysis (EA) of DCDBA*x* samples.

	N (wt.%)	**C (wt.%)**	**H (wt.%)**	**O (wt.%)**	**C/N (at.)**
DCDBA2	47.32	34.28	2.13	6.26	0.84
DCDBA5	47.56	33.83	2.34	9.26	0.83
DCDBA10	49.51	33.54	2.69	12.20	0.76
DCDBA20	50.34	34.56	3.31	10.18	0.80

Table S3. Lifetime calculation (triexponential fitting) for different CN materials.

Sample	τ_1 (ns)	A_1	τ_2 (ns)	A_2	τ_3 (ns)	A_3	Lifetime (ns)
DCDBA5	24.60	16.19	5.539	55.76	1.641	28.05	15.4
DCDBA20	3.372	45.88	17.527	12.75	0.747	41.37	10.9

Table S4. Comparison to other recently reported HER photocatalysts.

Photocatalyst	Light source	Reaction conditions[a]	H_2 generation rate (μmol g^{-1} h^{-1})	AQE {λ}	Ref.
PHI/K^+Cl^-	**>410 nm**	3 wt.% Pt, 10 vol.% TEOA	**11,449**	**15.6% {405 nm}**	**This work**
NaK-CN	>410 nm	3 wt.% Pt, 10 vol.% TEOA	270	9.8% {405 nm}	1
modified CN	>410 nm	3 wt.% Pt, 10 vol.% TEOA	925	4% {405 nm}	2
π-electron conjugated porous CN rods	>410 nm	3 wt.% Pt, 10 vol.% TEOA	10,160	20.0% {405 nm}	3
CN-2-Cl-mlm	>410 nm	3 wt.% Pt, 10 vol.% TEOA	8,952	9.05% {405 nm}	4
porous CN rods	>410 nm	3 wt.% Pt, 10 vol.% TEOA	4764	6.8% {405 nm}	5
PHI	>420 nm	3 wt.% Pt, 10 vol.% TEOA	44	5.4% {420 nm}	6
hybrid PHI/PTI copolymer	>420 nm	3 wt.% Pt, 10 vol.% TEOA	348.5	42% {420 nm}	6
Pt/g-C_3N_4	≥420 nm	10 vol.% CH_3OH	473.83	—	7
PtS/g-C_3N_4	≥420 nm	10 vol. % TEOA	1,072.6	45.7% {420 nm}	8
Pd/g-C_3N_4	>400 nm	10 vol. %TEOA	1,208.6	3.8% {420 nm}	9
RuP_x/g-C_3N_4	300 W Xe	10 vol. %TEOA	1,940	0.20% {420 nm}	10
Co_3O_4/g-C_3N_4	Visible	10 vol. %TEOA	50	—	11
MoP/g-C_3N_4	>400 nm	3 wt. % Pt, 10 vol. % TEOA	3,868	21.6% {405 nm}	12

Ni-MoS_x/g-C_3N_4	≥400 nm	5 wt. % Ni, 10 vol. % TEOA	5,968	—	13
C_{60}/g-C_3N_4	≥420 nm	3 wt. % Pt, 17 vol. % TEOA	870	—	14
Cu/$ZnIn_2S_4$	300 W Xe	ascorbic acid	9,864.7	—	15
Crystalline g-C_3N_4	300 W Xe	3 wt. % Pt, 10 vol.% TEOA	3,550.2	25% {420 nm}	16
$NiCo_2S_4$/ZIS-5	≥420 nm	TEOA	6,834.6	13% {400 nm}	17
CTFs	AM 1.5	3 wt.% Pt, 10 vol.% TEOA	6,595	2.11% {AM 1.5}	18
$Cu_3Mo_2O_9$/TiO_2	300 W Xe	20 vol.% TEOA	3,401.9	—	19

[a]Triethanolamine (TEOA), ascorbic acid, and methanol, if listed, act as hole scavengers.

Table S5. Effective electron masses (m_e*/m_0) in the [100] and [002] directions of different CN structures based on DFT calculation.

CN type	Effective e^- mass (m_e*/m_0)
Bulk CN [100]	0.9125
Bulk CN [002]	2.3785
PTI [100]	0.8204
PTI [002]	2.2869
PHI [100]	0.9279
PHI [002]	6.5293

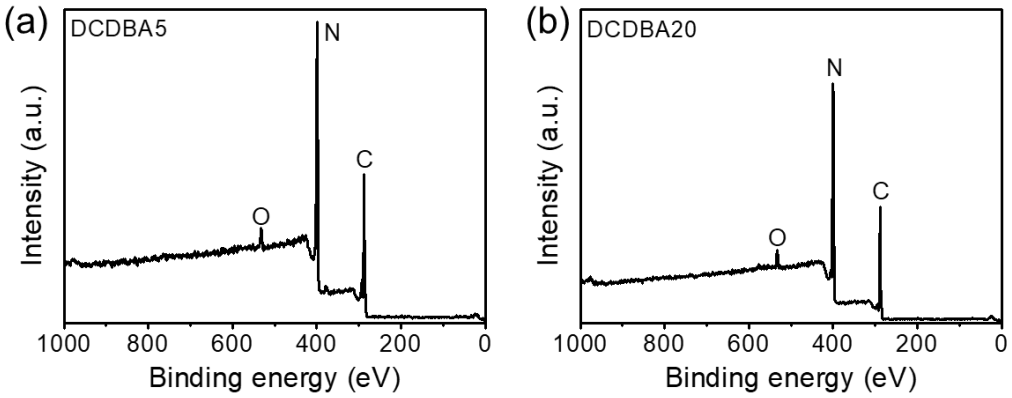

Figure S1. XPS wide survey spectra of (a) DCDBA5 and (b) DCDBA20.

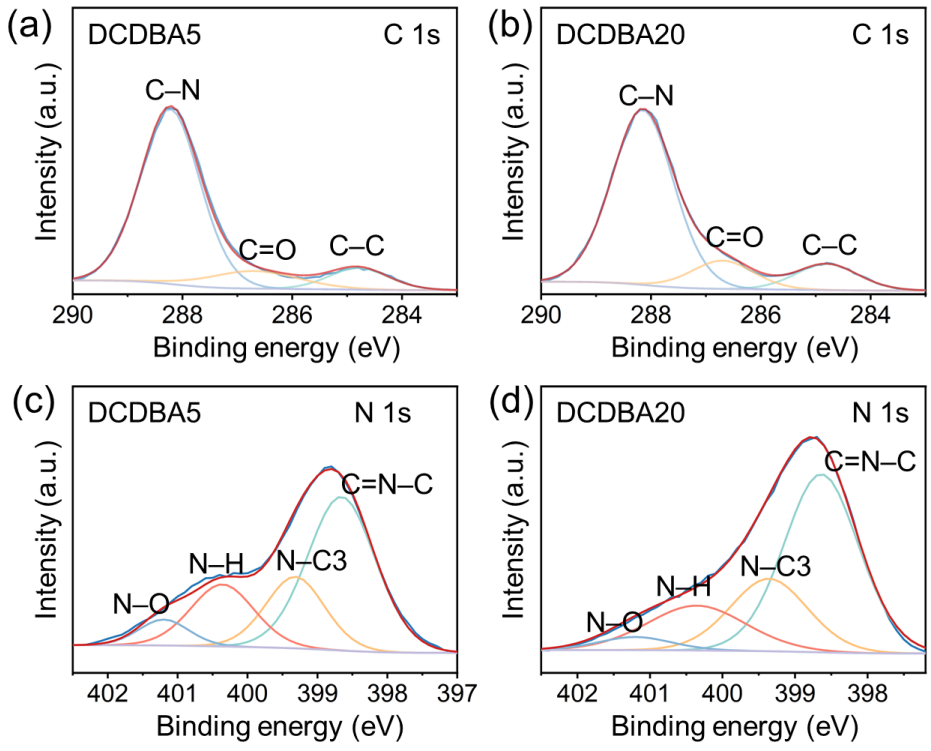

Figure S2. XPS spectra of samples obtained at salt:reactants mass ratios of 5:1 and 20:1. C 1s edge: (a) DCDBA5, (b) DCDBA20; N 1s edge: (c) DCDBA5, (d) DCDBA20. Experimental: blue spectra; fitted: red curve; deconvoluted peaks are labeled.

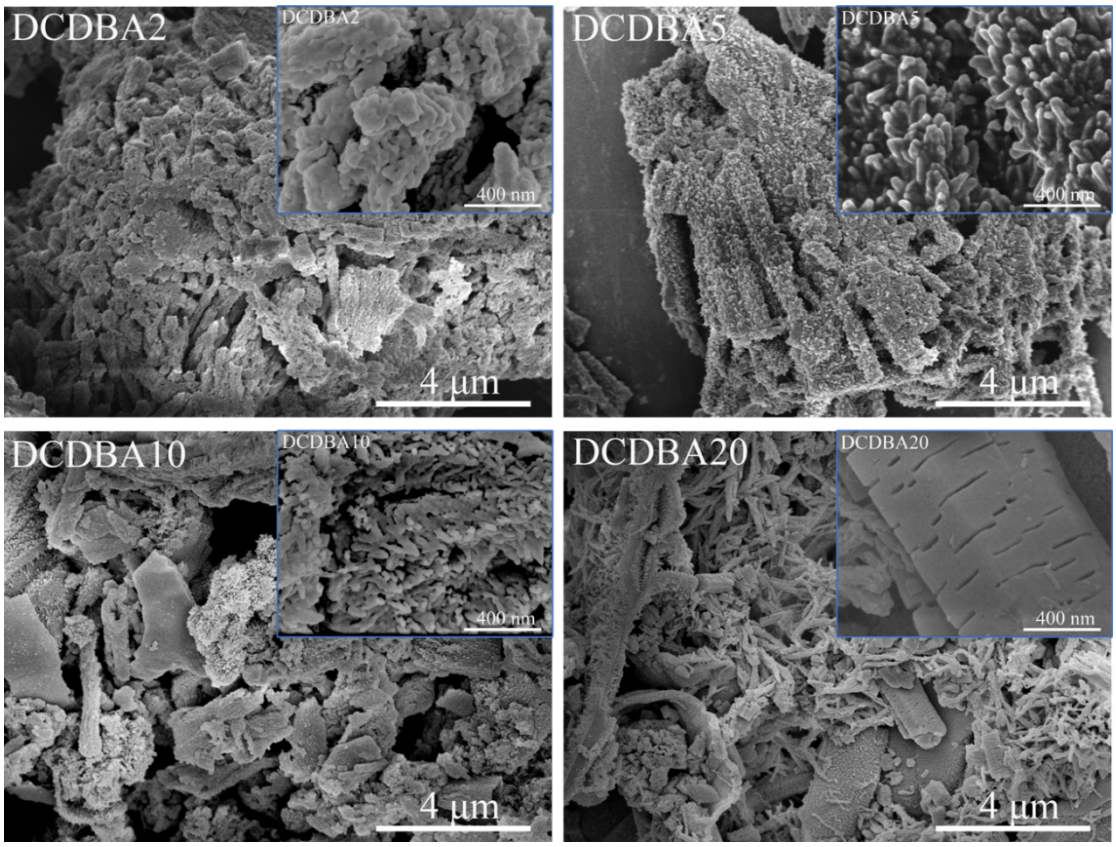

Figure S3. SEM images of DCDBA*x* samples. Insets are higher-magnification images of the corresponding sample.

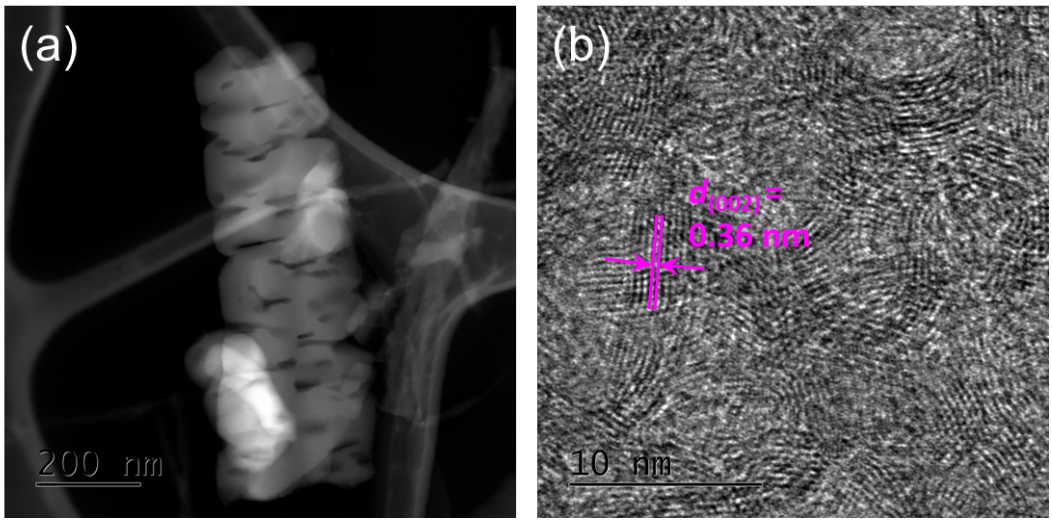

Figure S4. TEM and HRTEM images of DCDBA20.

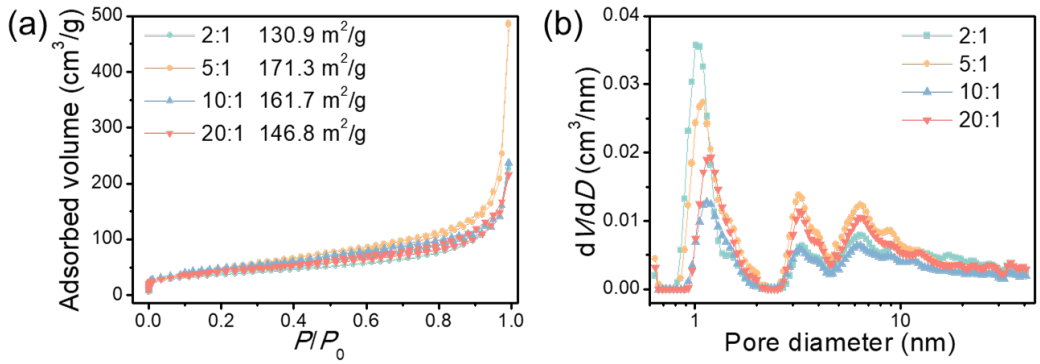

Figure S5. (a) N_2 adsorption-desorption isotherms at 77 K and (b) corresponding calculated pore size (diameter, D) distributions using a density functional theory (DFT) model of DCDBAx samples. The indicated specific surface areas (S_A) are obtained using a five-point linear fitting of the adsorption branch at $P < 0.3P_0$ according to the Brunauer–Emmett–Teller (BET) model.

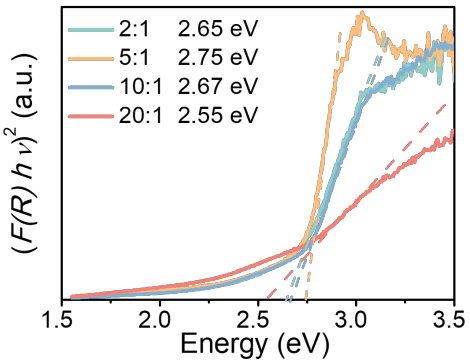

Figure S6. Tauc plots corresponding to UV–vis spectra, assuming a direct optical band gap (E_g). The estimated E_g values are listed in the legend.

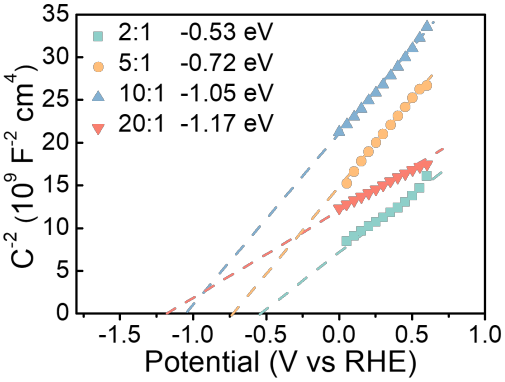

Figure S7. Mott-Schottky curves of DCDBA*x* samples.

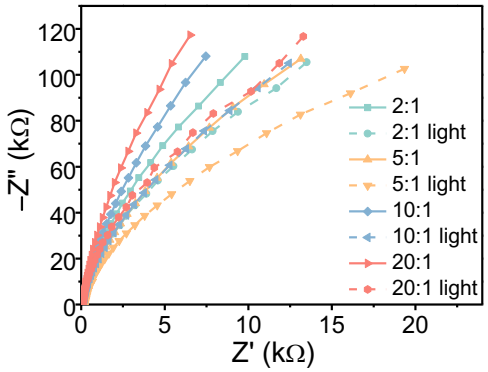

Figure S8. Nyquist EIS plots of DCDBA*x* samples.

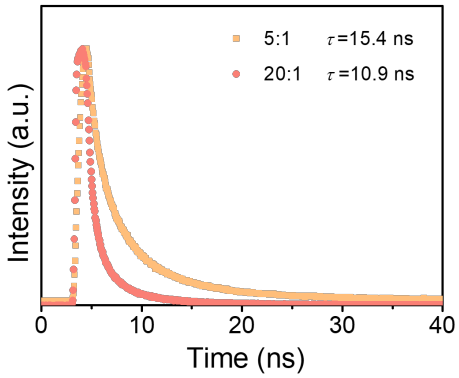

Figure S9. Transient fluorescence spectra (λ_{ex} = 370 nm) of DCDBA5 and DCDBA20. (The average fluorescence lifetime was obtained by triexponential fitting, see Table S3).

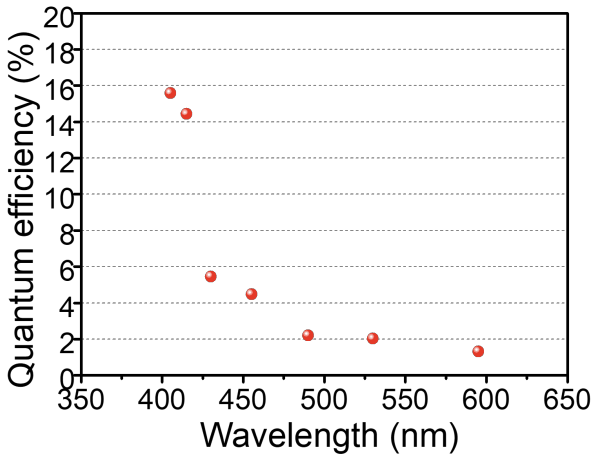

Figure S10. Wavelength-dependent apparent quantum efficiency (AQE) for HER using DCDBA5 as the photocatalyst.

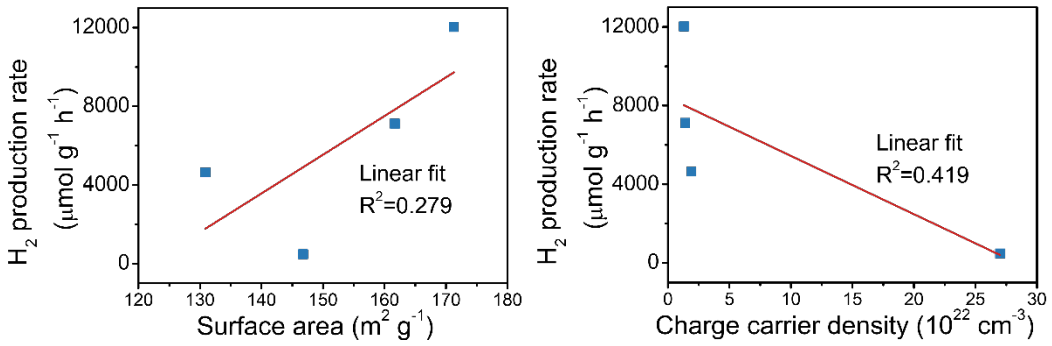

Figure S11. Linear fitting (using least-squares regression) between the measured photocatalytic HER activities and the specific surface area (left), and charge carrier density (right) of DCDAB*x* samples.

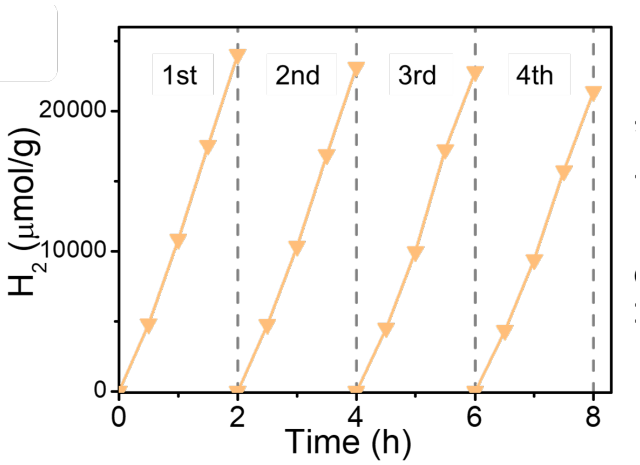

Figure S12. Stability of HER using DCDBA5.

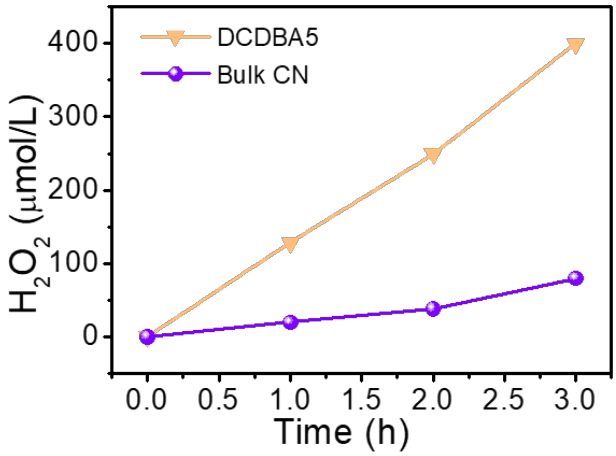

Figure S13. Time-production plots of H_2O_2 generated by photocatalysis over DCDBA5 and bulk CN (prepared by pyrolysis of DCD for 4 h at 500 °C).

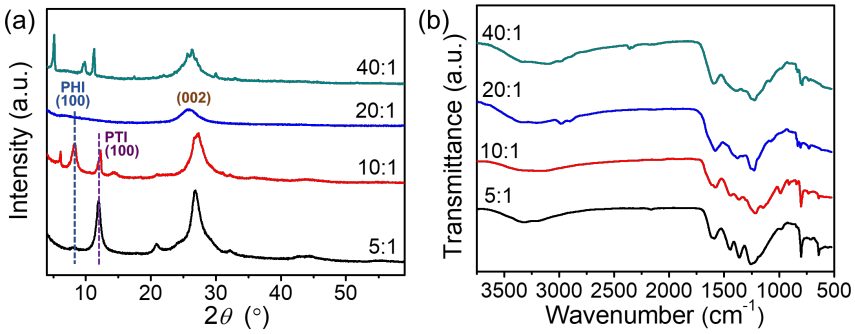

Figure S14. (a) XRD patterns and (b) FTIR spectra of DCDTAP*x*. The samples were obtained from different salt:reactants mass ratios *x* between KCl/LiBr salts and reactants (DCD and TAP in this case), specifically 5:1, 10:1, 20:1, and 40:1. The patterns and spectra are vertically offset for clarity.

The XRD patterns of the samples obtained from precursor mixtures at salt:reactants mass ratios of 5:1 and 10:1 exhibit diffraction peaks around 27° and 12°, corresponding to the stacking of triazine rings, indexed as (002), and the in-plane structural motif, indexed as (100), respectively, of carbon nitride; a small shift when a higher salt:reactants ratio is used can be ascribed to the intercalation of salt ions within the CN structure.[20,21] As with the DCDBA*x* samples, there is a notable peak at 8°, which can be assigned to the (100) plane of poly(heptazine imide) (PHI) structure. The FTIR (Figure S8b) analysis also confirms the formation of a polymeric carbon nitride structure with vibration bands at 806 cm^{-1} (triazine group), 1200–1700 cm^{-1} (CN heterocyclic units), and 2900–3500 cm^{-1} (N–H).

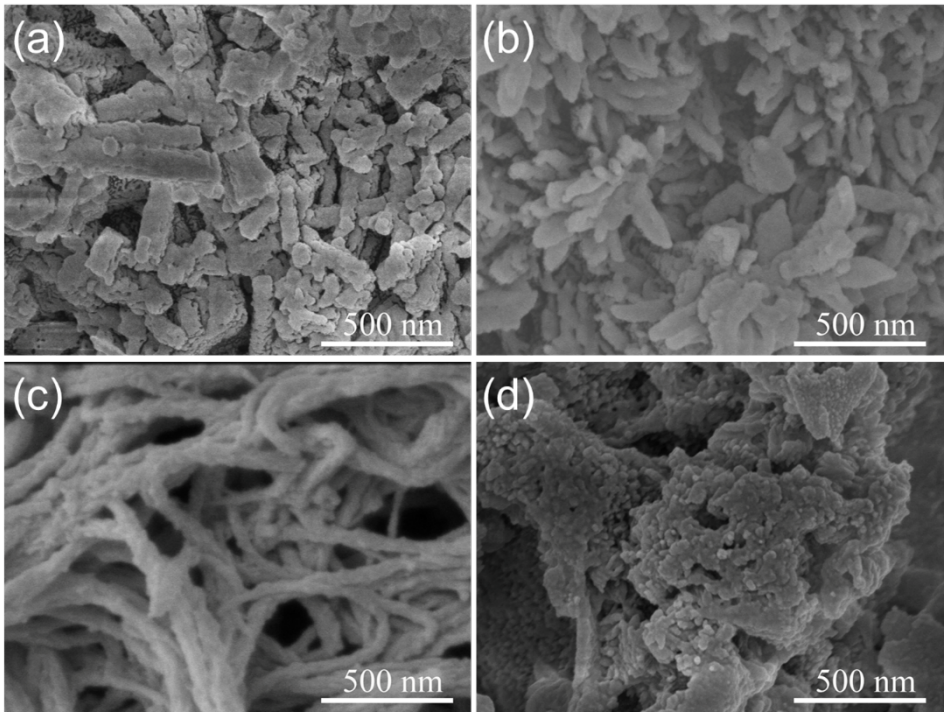

Figure S15. SEM images of (a) DCDTAP5, (b) DCDTAP10, (c) DCDTAP20, and (d) DCDTAP40.

The samples exhibit an elongated rod-like structure composed of irregular small particles.

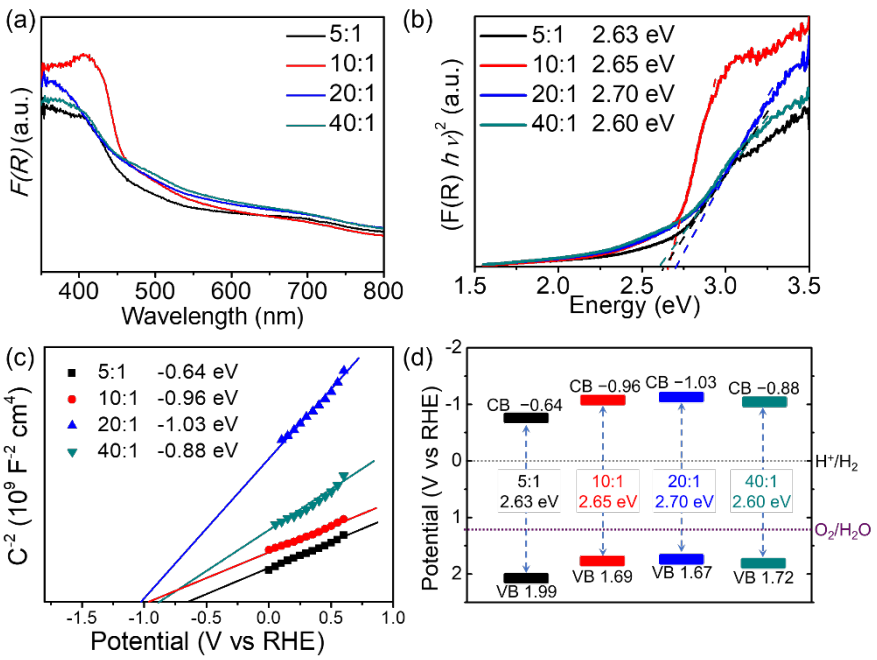

Figure S16. Energy bands determination of DCDTAP*x* samples. (a) UV–vis spectra of the powders, measured using a diffuse reflectance accessory (DRA), showing the Kubelka-Munk *F*(*R*) function (proportional to absorbance). (b) The corresponding Tauc plots, assuming a direct optical band gap and its estimation,[22] (c) Mott-Schottky curves. (d) Calculated energy band schemes (assuming flat band potential ≈ CB).

The studied optical properties indicate a similar absorption edge for all samples. The optical band gaps (E_g) estimation using Tauc plots (assuming a direct E_g) are 2.63, 2.65, 2.70, and 2.60 eV for DCDTAP5, DCDTAP10, DCDTAP20, and DCDTAP40, respectively—substantially the same as powders of "common" melon-based carbon nitride (ca. 2.7 eV).[23] The proposed energy band alignments confirm that the energy band positions of the materials are suitable for water-splitting.

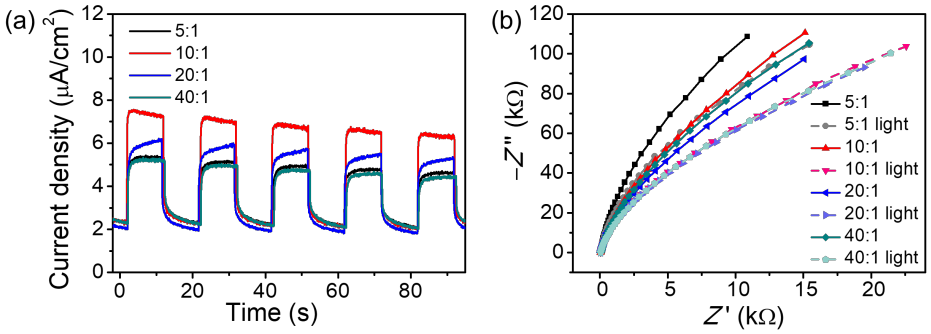

Figure S17. (a) Transient photocurrent responses and (b) Nyquist electrochemical impedance spectroscopy (EIS) plots for DCDTAP*x* samples.

The photocurrent density of DCDTAP10 (10:1, red trace) is the highest at 1.23 V vs RHE; in the first illumination cycle, it exceeds a photocurrent density ($j_{\text{illumination}} - j_{\text{dark}}$) of 5 μA cm^{-2}, implying it has the best charge separation efficiency among all prepared DCDTAP*x* materials. Additionally, the arc radii of the EIS Nyquist plots of DCDTAP10, DCDTAP20, and DCDTAP40 are considerably smaller than that of DCDTAP5, indicating their lower charge transfer resistances (R_{CT}).

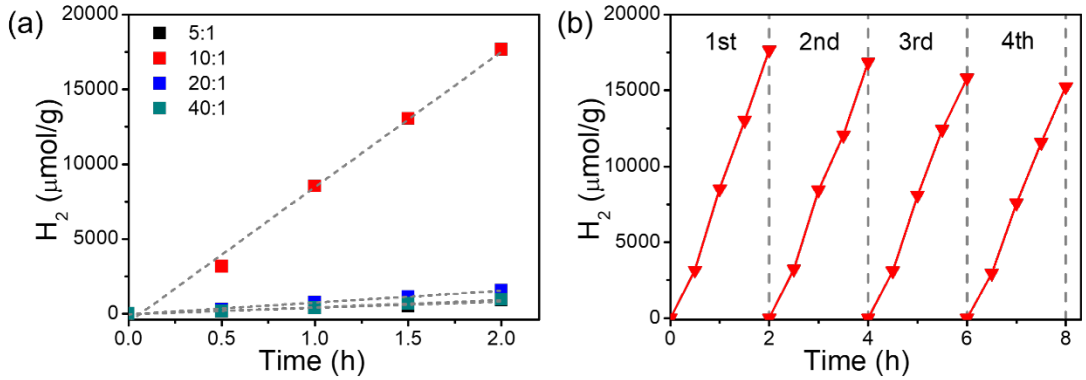

Figure S18. (a) H_2(g) production over time from the photocatalytic HER over DCDTAP*x*, normalized to the photocatalyst mass. (b) Stability and recyclability of the catalytic H_2 evolution using DCDTAP10, showing four subsequent 2 h reactions.

The photocatalytic HER experiments on DCDTAP*x* photocatalysts were conducted under constant visible-light illumination (white light LED, $\lambda \geq 410$ nm) of the reaction vessel for 2 h. DCDTAP10 shows the highest photocatalytic activity (8.474 mmol g^{-1} h^{-1}). To test the photocatalytic stability of DCDTAP10, the same sample was reused during four consecutive 2 h cycles. No significant attenuation in the HER rate was observed upon reuse.

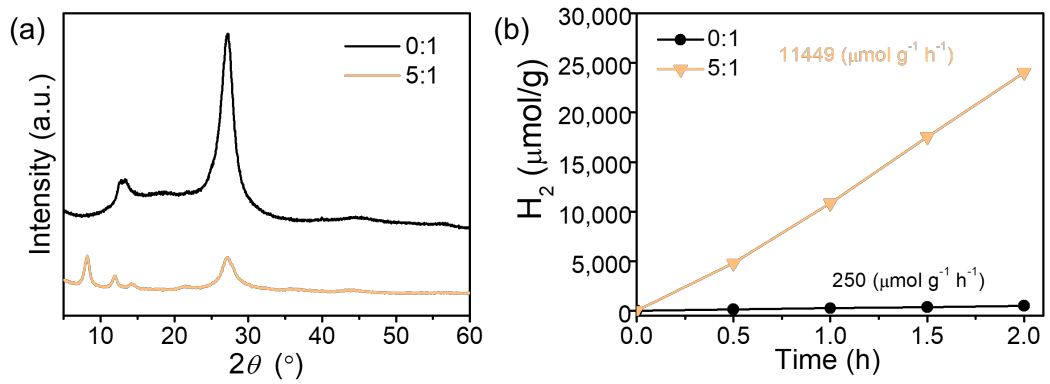

Figure S19. (a) XRD patterns and (b) H_2 generation from photocatalytic HER over photocatalysts obtained by a solid-state reaction (thermal polymerization of the precursors without a salt, black trace) and, for comparison (orange), a DCDBA5 sample (from a molten salt synthesis).

When a CN is prepared without using a salt medium (named 0:1 since there is no salt, only DCD and BA precursors), the XRD pattern shows two main diffraction signals at ca. 27° and 13°, which correspond to the (002) and (100) plane of melon-based carbon nitride.[23] There is no peak at $2\theta = 8°$, indicating that the salt medium plays an important role in the formation of the reported PHI structure.

The photocatalytic hydrogen evolution rate is about 250 μmol g^{-1} h^{-1}, which is much lower than that of DCDBA5, the best-performing PHI photocatalyst (11,449 μmol g^{-1} h^{-1}), and that of DCDBA20, a PTI photocatalyst prepared in the salt medium (455 μmol g^{-1} h^{-1}).

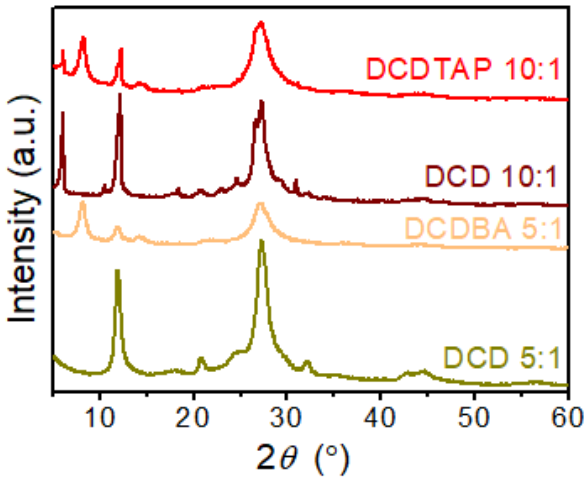

Figure S20. XRD patterns of samples obtained from a single precursor (DCD) and mixed precursors (DCD+BA or DCD+TAP) in a molten salt synthesis at salt:reactant mass ratios of 5:1 and 10:1.

Using only DCD as a single precursor and salt:DCD mass ratios of 5:1 and 10:1 results in CN materials showing no diffraction signal at $2\theta = 8°$. Their photocatalytic hydrogen evolution rates (135 μmol g^{-1} h^{-1} for DCD 10:1) are also much lower than that of the corresponding sample prepared using mixed precursors; this difference indicates that the assembled supramolecular precursors play a crucial role in the formation of this PHI structure.

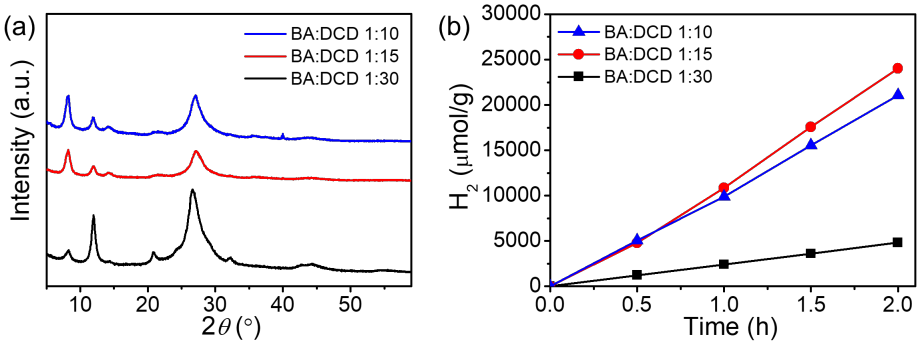

Figure S21. (a) XRD patterns and (b) H_2 generation over time from the photocatalytic HER over CN samples obtained with different BA-to-DCD molar proportions (1:30, 1:15, 1:10) in the molten salt medium at salt:reactant mass ratios of 5:1.

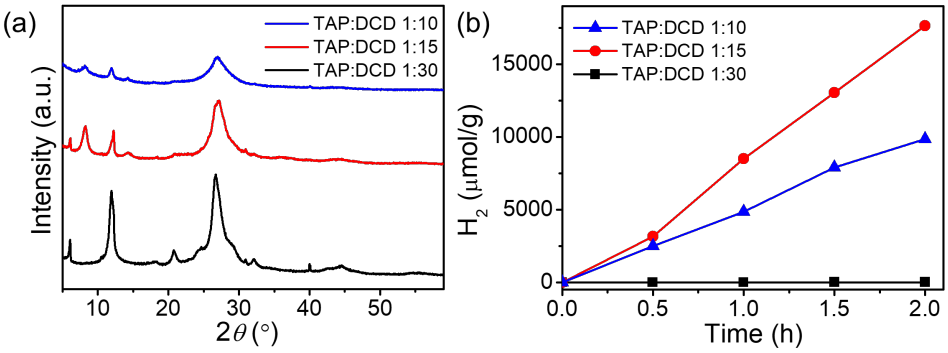

Figure S22. (a) XRD patterns and (b) photocatalytic H_2 production over time from HER over CN samples obtained from different TAP-to-DCD molar proportions (1:30, 1:15, 1:10) in the molten salt medium at a salt:reactants mass ratio of 10:1.

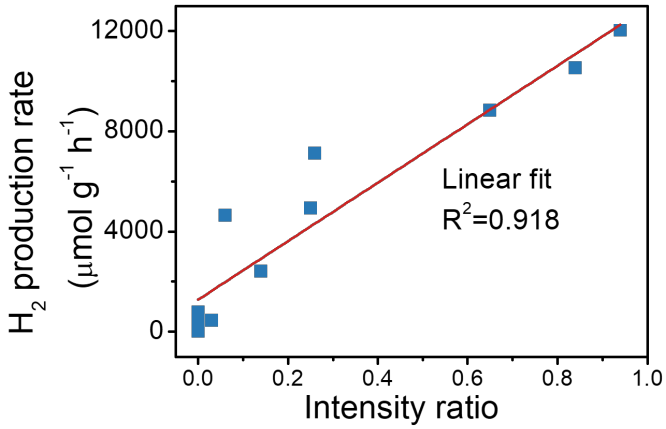

Figure S23. Linear fitting (using least-squares regression) between the measured photocatalytic HER activities and the XRD diffraction intensity ratios (ratio between the signal at $2\theta = 8°$ and $2\theta = 27°$ for each sample).

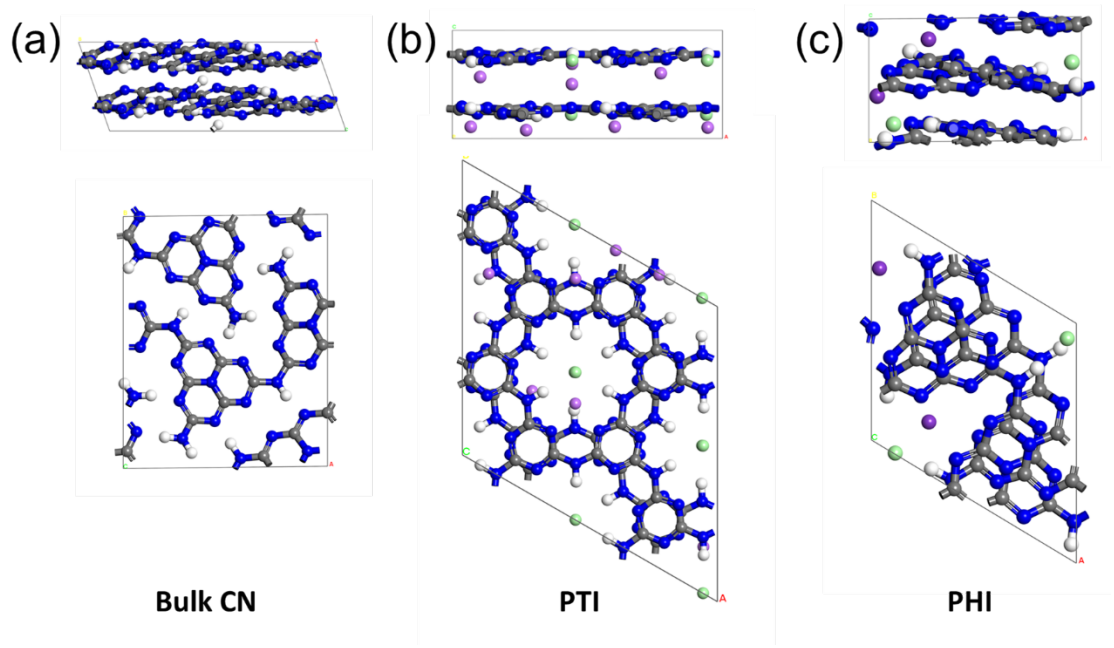

Figure S24. System models of the three CN materials: (a) melon-based bulk CN (BCN), (b) poly(triazine) imine (PTI), and (c) poly(heptazine) imine (PHI). Atom color code: purple: K^+, green: Cl^-, gray: C, blue: N, white: H.

Supporting Information References

(1) J. Barrio, S. Barzilai, N. Karjule, P. Amo-Ochoa, F. Zamora, M. Shalom, Synergistic Doping and Surface Decoration of Carbon Nitride Macrostructures by Single Crystal Design, ACS Applied Energy Materials. 4 (2021) 1868–1875. https://doi.org/10.1021/acsaem.0c02964.

(2) N. Karjule, J. Barrio, J. Tzadikov, M. Shalom, Electronic Structure Engineering of Carbon Nitride Materials by Using Polycyclic Aromatic Hydrocarbons, Chemistry - A European Journal. 26 (2020) 6622–6628. https://doi.org/10.1002/chem.201905875.

(3) J. Xia, N. Karjule, G. Mark, M. Volokh, H. Chen, M. Shalom, Aromatic alcohols oxidation and hydrogen evolution over π-electron conjugated porous carbon nitride rods, Nano Research. (2022). https://doi.org/10.1007/s12274-022-4717-4.

(4) G. Mark, S. Mondal, M. Volokh, J. Xia, M. Shalom, Halogen–Hydrogen Bonding for the Synthesis of Efficient Polymeric Carbon-Nitride Photocatalysts, Solar RRL. 6 (2022). https://doi.org/10.1002/solr.202200834.

(5) J. Xia, G. Mark, M. Volokh, Y. Fang, H. Chen, X. Wang, M. Shalom, Supramolecular organization of melem for the synthesis of photoactive porous carbon nitride rods, Nanoscale. 13 (2021) 19511–19517. https://doi.org/10.1039/d1nr06974h.

(6) J. Zhang, X. Liang, C. Zhang, L. Lin, W. Xing, Z. Yu, G. Zhang, X. Wang, Improved Charge Separation in Poly(heptazine-triazine) Imides with Semi-coherent Interfaces for Photocatalytic Hydrogen Evolution, Angewandte Chemie - International Edition. 61 (2022). https://doi.org/10.1002/anie.202210849.

(7) Y. Zhu, T. Wang, T. Xu, Y. Li, C. Wang, Size effect of Pt co-catalyst on photocatalytic efficiency of g-C_3N_4 for hydrogen evolution, Applied Surface Science. 464 (2019) 36–42. https://doi.org/10.1016/j.apsusc.2018.09.061.

(8) B. Lin, Y. Zhou, B. Xu, C. Zhu, W. Tang, Y. Niu, J. Di, P. Song, J. Zhou, X. Luo, L. Kang, R. Duan, Q. Fu, H. Liu, R. Jin, C. Xue, Q. Chen, G. Yang, K. Varga, Q. Xu, Y. Li, Z. Liu, F. Liu, 2D PtS nanorectangles/g-C_3N_4 nanosheets with a metal sulfide-support interaction effect for high-efficiency photocatalytic H_2 evolution, Materials Horizons. 8 (2021) 612–618. https://doi.org/10.1039/d0mh01693d.

(9) Z. Mo, H. Xu, X. She, Y. Song, P. Yan, J. Yi, X. Zhu, Y. Lei, S. Yuan, H. Li, Constructing Pd/2D-C_3N_4 composites for efficient photocatalytic H_2 evolution through nonplasmon-induced bound electrons, Applied Surface Science. 467–468 (2019) 151–157. https://doi.org/10.1016/j.apsusc.2018.10.115.

(10) J. Zhang, Q. Zhu, Y. Ma, L. Wang, M. Nasir, J. Zhang, Photo-generated charges escape from P+ center through the chemical bridges between P-doped g-C_3N_4 and RuxP nanoparticles to enhance the photocatalytic hydrogen evolution, Catalysis Today. 380 (2021) 223–229. https://doi.org/10.1016/j.cattod.2020.12.037.
(11) L. Yang, J. Liu, L. Yang, M. Zhang, H. Zhu, F. Wang, J. Yin, Co_3O_4 imbedded g-C3N4 heterojunction photocatalysts for visible-light-driven hydrogen evolution, Renewable Energy. 145 (2020) 691–698. https://doi.org/10.1016/j.renene.2019.06.072.
(12) G. Zuo, Y. Wang, W.L. Teo, A. Xie, Y. Guo, Y. Dai, W. Zhou, D. Jana, Q. Xian, W. Dong, Y. Zhao, Ultrathin $ZnIn_2S_4$ Nanosheets Anchored on Ti3C2TX MXene for Photocatalytic H_2 Evolution, Angewandte Chemie - International Edition. 59 (2020) 11287–11292. https://doi.org/10.1002/anie.202002136.
(13) B. Wang, X. Li, H. Wu, G. Xu, X. Zhang, X. Shu, J. Lv, Y. Wu, Synthesis of Ni−MoSx/g-C3N4 for Photocatalytic Hydrogen Evolution under Visible Light, ChemCatChem. 12 (2020) 911–916. https://doi.org/10.1002/cctc.201901654.
(14) D. Long, W. Chen, X. Rao, S. Zheng, Y. Zhang, Synergetic effect of C60/g-C_3N_4 nanowire composites for enhanced photocatalytic H2 evolution under visible light irradiation, ChemCatChem. 12 (2020) 2022–2031. https://doi.org/10.1002/cctc.201901958.
(15) S. Zhang, Z. Zhang, Y. Si, B. Li, F. Deng, L. Yang, X. Liu, W. Dai, S. Luo, Gradient Hydrogen Migration Modulated with Self-Adapting S Vacancy in Copper-Doped $ZnIn_2S_4$ Nanosheet for Photocatalytic Hydrogen Evolution, ACS Nano. 15 (2021) 15238–15248. https://doi.org/10.1021/acsnano.1c05834.
(16) Z. Yu, X. Yue, J. Fan, Q. Xiang, Crystalline Intramolecular Ternary Carbon Nitride Homojunction for Photocatalytic Hydrogen Evolution, ACS Catalysis. 12 (2022) 6345–6358. https://doi.org/10.1021/acscatal.2c01563.
(17) Y. Guo, L. Mao, Y. Tang, Q. Shang, X. Cai, J. Zhang, H. Hu, X. Tan, L. Liu, H. Wang, T. Yu, J. Ye, Concentrating electron and activating H-OH bond of absorbed water on metallic $NiCo_2S_4$ boosting photocatalytic hydrogen evolution, Nano Energy. 95 (2022). https://doi.org/10.1016/j.nanoen.2022.107028.
(18) H. Ye, N. Gong, Y. Cao, X. Fan, X. Song, H. Li, C. Wang, Y. Mei, Y. Zhu, Insights into the Role of Protonation in Covalent Triazine Framework-Based Photocatalytic Hydrogen Evolution, Chemistry of Materials. 34 (2022) 1481–1490. https://doi.org/10.1021/acs.chemmater.1c02697.

(19) W. Huang, Z. Fu, X. Hu, Q. Wang, J. Fan, E. Liu, Efficient photocatalytic hydrogen evolution over Cu3Mo2O9/TiO2 p-n heterojunction, Journal of Alloys and Compounds. 904 (2022) 164089. https://doi.org/10.1016/j.jallcom.2022.164089.
(20) M.J. Bojdys, J.O. Müller, M. Antonietti, A. Thomas, Ionothermal synthesis of crystalline, condensed, graphitic carbon nitride, Chemistry - A European Journal. 14 (2008) 8177–8182. https://doi.org/10.1002/chem.200800190.
(21) L. Tian, J. Li, F. Liang, J. Wang, S. Li, H. Zhang, S. Zhang, Molten salt synthesis of tetragonal carbon nitride hollow tubes and their application for removal of pollutants from wastewater, Applied Catalysis B: Environmental. 225 (2018) 307–313. https://doi.org/10.1016/j.apcatb.2017.11.082.
(22) P. Makuła, M. Pacia, W. Macyk, How To Correctly Determine the Band Gap Energy of Modified Semiconductor Photocatalysts Based on UV-Vis Spectra, Journal of Physical Chemistry Letters. 9 (2018). https://doi.org/10.1021/acs.jpclett.8b02892.
(23) X. Wang, K. Maeda, A. Thomas, K. Takanabe, G. Xin, J.M. Carlsson, K. Domen, M. Antonietti, A metal-free polymeric photocatalyst for hydrogen production from water under visible light, Nature Materials. 8 (2009) 76–80. https://doi.org/10.1038/nmat2317.